doi:10.26443/seismica.v5i2.2557

Dense Seismic Array Monitoring of the Glacier Tongue of Isunnguata Sermia, West Greenland

Nicolas Paris *[1], **Florent Gimbert** [1], **Tifenn Le Bris** [1], **Stephen J. Livingstone** [2], **Samuel H. Doyle** [2,3], **Alexandre Michel** [1], **Andrew J. Sole** [2], **Albanne Lecointre** [4], **Laura Pinzon-Rincon** [5], **Gregor Hillers** [6], **Roméo Courbis** [6], **Philippe Roux** [4], **Guilhem Barruol** [1], **Elizabeth A. Bagshaw** [7], **Thomas R. Chudley** [7,8], **Lisa Craw** [9], **Laura A. Edwards** [10], **Adrien Gilbert** [1], **Jonathan D. Hawkins** [9], **Ryan N. Ing** [11], **Andrew H. Jones** [12], **Angus Moffat** [2], **Matthew W. Peacey** [3,7], **Michael R. Prior-Jones** [9], **Neil Ross** [13], **Arnaud Reboud** [1], **Robert D. Storrar** [14], **Sian C. Thorpe** [2], **Remy Veness** [12], **Tun Jan Young** [15]

[1]Université Grenoble Alpes, CNRS, INRAE, IRD, Grenoble INP, IGE, Grenoble, France, [2]School of Geography and Planning, University of Sheffield, Sheffield, UK, [3]Centre for Glaciology, Department of Geography and Earth Sciences, Aberystwyth University, Aberystwyth, SY23 3DB, UK, [4]ISTerre, Université Grenoble Alpes, CNRS, Université Savoie Mont Blanc, IRD, Université Gustave Eiffel, Grenoble, France, [5]German Research Centre for Geosciences (GFZ), Potsdam, Germany, [6]Institute of Seismology, Department of Geosciences and Geography, University of Helsinki, Helsinki, Finland, [7]School of Geographical Sciences, University of Bristol, University Road, Bristol BS8 1SS, UK, [8]Department of Geography, Durham University, Durham, UK, [9]School of Earth and Environmental Sciences, Cardiff University, Cardiff, GB, [10]School of Biological and Environmental Sciences, Liverpool John Moores University, Liverpool, UK, [11]School of Geosciences, University of Edinburgh, Edinburgh, UK, [12]Institute of Social Sciences: Geography, Environment and Planning, Sheffield Hallam University, Sheffield, UK, [13]School of Geography, Politics and Sociology, Newcastle University, Newcastle upon Tyne, UK, [14]Department of the Natural and Built Environment, Sheffield Hallam University, Sheffield, UK, [15]School of Geography and Sustainable Development, University of St Andrews, St Andrews, UK

Author contributions: *Conceptualization*: Florent Gimbert, Stephen J. Livingstone, Andrew J. Sole, Samuel H. Doyle, Nicolas Paris. *Methodology*: Nicolas Paris, Florent Gimbert, Tifenn Le Bris, Albanne Lecointre, Laura Pinzon-Rincon, Philippe Roux, Guilhem Barruol. *Visualization*: Nicolas Paris. *Data Curation*: Nicolas Paris, Alexandre Michel. *Resources*: Florent Gimbert, Alexandre Michel, Tifenn Le Bris, Philippe Roux, Samuel H. Doyle, Stephen J. Livingstone, Guilhem Barruol, Sian C. Thorpe, Thomas R. Chudley, Matthew W. Peacey, Michael R. Prior-Jones, Adrien Gilbert, Ryan N. Ing, Laura Pinzon-Rincon, Laura A. Edwards, Andrew H. Jones, Elizabeth A. Bagshaw, Angus Moffat, Lisa Craw, Jonathan D. Hawkins, Neil Ross, Arnaud Reboud, Robert D. Storrar, Tun Jan Young, Roméo Courbis, Gregor Hillers. *Writing - Original draft*: Nicolas Paris, Florent Gimbert. *Writing - Review & Editing*: Nicolas Paris, Samuel H. Doyle, Gregor Hillers, Stephen J. Livingstone, Ryan N. Ing, Alexandre Michel, Florent Gimbert, Thomas R. Chudley, Neil Ross, Albanne Lecointre, Tifenn Le Bris, Andrew J. Sole, Sian C. Thorpe, Guilhem Barruol. *Project administration*: Florent Gimbert, Stephen J. Livingstone. *Funding acquisition*: Florent Gimbert, Stephen J. Livingstone, Laura A. Edwards, Elizabeth A. Bagshaw, Neil Ross, Andrew J. Sole, Robert D. Storrar, Michael R. Prior-Jones.

Abstract Accelerating mass loss from the Greenland Ice Sheet is affected by meltwater-driven changes in ice dynamics, which remain poorly understood due to limited observations. Here, we present a 2.5 km^2 wide dense passive seismic array experiment conducted in the ablation zone of Isunnguata Sermia, West Greenland. We target varying surface melt conditions through one-month long monitoring periods in spring, summer, and fall using 82–117 nodes deployed in 2023 and 2024 complemented by multi-week surface Distributed Acoustic Sensing acquisitions in 2024. We assess data quality using power spectral densities and noise correlation functions. We find that low-frequency seismic power is highly correlated to ice surface velocity, suggesting a strong control of subglacial hydrology on ice dynamics. We retrieve stable and high signal-to-noise ratio noise correlations containing Rayleigh, Love, and P wave arrivals, suggesting these may successfully be used for glacier structure imaging and monitoring. We finally demonstrate we can locate numerous seismic events with resolution down to a few meters using Matched Field Processing and which exhibit characteristic spatial patterns evolving across seasons. These findings establish the potential of such experiment to infer glacier hydrology, dynamics, and structure at high spatial and temporal resolution.

Production Editor:
Andrea Llenos
Handling Editor:
György Hetenyi
Copy & Layout Editor:
Hannah F. Mark

Received:
January 27, 2026
Accepted:
June 29, 2026
Published:
July 17, 2026

1 Introduction

The Greenland Ice Sheet is losing mass at an accelerating pace due to climate warming, making it a major contributor to global sea level rise (Mouginot et al., 2019; Rignot et al., 2019). The increase in ice loss results from enhanced surface ablation through melting and faster ice flow, leading to higher rates of ice discharge into the ocean (Mouginot et al., 2019). Earlier research identified surface meltwater as a primary control on ice dynamics (Zwally et al., 2002; Schoof, 2010; Andrews et al., 2014). Water from surface melt can access the ice bed through crevasses and moulins (Andrews et al., 2014) and modify glacier basal sliding velocity by lubricating the ice-bed interface (Lliboutry, 1968; Schoof, 2005; Gagliardini et al., 2007). However, the processes that control the transit of water to the bed, the lubrication of the ice-bed interface and its links to the characteristics of meltwater and glaciers remain poorly understood due to limited observations.

Water throughout the ice column and at the ice-bed interface is expected to be stored or conveyed through highly heterogeneous structures spanning a wide range

*Corresponding author: nicolas.paris3@univ-grenoble-alpes.fr

of spatial scales. These include crevasses (Nath and Vaughan, 2003), whose openings can range from millimeters to meters; moulins (Andrews et al., 2014), whose diameters can vary from centimeters to meters; meter-scale structures such as subglacial channels (Flowers, 2015; Gimbert et al., 2016) and water-filled cavities (Gagliardini et al., 2007); and kilometer-scale structures such as lakes (Livingstone et al., 2019). Determining the impact of surface melt water on ice dynamics requires resolving this multi-scale spatial complexity and its evolution through time, a task that is challenging to achieve using traditional observational methods. The broad applicability of water pressure measurements in boreholes is limited by their discrete nature, as numerous boreholes must be drilled through the ice to the bed to resolve the spatial heterogeneity of the subglacial drainage system (e.g. Murray and Clarke, 1995; Fudge et al., 2008; Meierbachtol et al., 2013; Rada and Schoof, 2018). Drilling is time-intensive, costly, and logistically-challenging to perform at scale in remote areas such as Greenland. Complementary constraints can be obtained from the combination of surface motion observations with physical models (Togaibekov et al., 2024) or with targeted hydrology measurements (Andrews et al., 2014; Chandler et al., 2013), but, being spatially integrative, these techniques do not allow the heterogeneous nature of these systems to be resolved.

Passive seismology uses continuous seismic ground motion generated by natural or anthropogenic sources. It offers an interesting prospect for high-resolution imaging and temporal monitoring of glacier structures in response to hydrological forcing. Tremors generated by subglacial water flow can be used to infer changes in channel flow properties, such as water pressure and conduit size (Gimbert et al., 2016). Seismic arrays and advanced signal processing techniques have been used on the Greenland Ice Sheet to detect various seismic sources (Jones et al., 2013; Röösli et al., 2014; Roeoesli et al., 2016). When sufficiently dense, these arrays can be used to locate flow through distributed to localized networks at spatial resolutions down to a few tens of meters (Lindner et al., 2020; Journeau et al., 2022; Nanni et al., 2021). Beyond source analysis, monitoring glacier structure using seismic noise interferometry has successfully retrieved changes in internal ice structure due to crevasses (Nanni et al., 2021) and in subglacial hydrological characteristics, such as the size and shape of cavities forming the distributed hydrological system (Zhan, 2019). Added monitoring capabilities are now provided by Distributed Acoustic Sensing (DAS), turning optical fibers, which are inexpensive and easy to deploy, into high frequency strain rate sensors that record the seismic wavefield along the cable (Booth et al., 2020; Fichtner et al., 2025; Walter et al., 2020). Although this technique holds great promise for glaciological applications, so far, only a limited number of studies have deployed optical fiber in glacier ablation zones (Manos et al., 2024), and questions remain unanswered about the optimal deployment strategy and data quality.

Previous studies have demonstrated the relevance of passive seismology in probing glaciers, but progress towards a better understanding of the links between melt-water and glacier dynamics in Greenland requires seismic experiments yielding high spatial resolution over representative spatial and temporal scales. The spatial scale covered by such an experiment should ideally correspond to that of the mesh scale in physical models, which is on the order of a few square kilometers (Maier et al., 2022). Achieving sub-wavelength sampling, necessary for high-resolution source localization and imaging, requires deploying roughly 50–200 sensors across the study area to meet the required sensor spacing of ∼40–400 m, given typical surface wave (2–20 Hz, 1600–1700 m/s) and P wave (≥40 Hz, 3600–3800 m/s) properties. The temporal scale should be long enough to experience varying surface melt conditions, which in glacier ablation zones spans the melt season, over which the glacier surface lowering is typically on the order of 2–6 m (Van den Broeke et al., 2017). Recovering high-quality seismic signals from tens to hundreds of stations deployed under such conditions is challenging, and requires a deployment strategy adapted to minimize sensor tilt.

Here we report on a dense seismic array experiment conducted on Isunnguata Sermia, West Greenland, intended to address the challenges outlined above. We deployed dense seismic arrays of 82–117 stations covering ∼2.5 km^2 during spring 2023 and in the summer and fall of 2024 in a high ablation zone. This region is highly crevassed, surface hydrology is intense in the summer, and subglacial hydrology is expected to incorporate key behaviors from water drainage through channels to water storage in expected subglacial lakes identified from previous surveys (Livingstone et al., 2019). We also conducted multi-week, nearly continuous DAS acquisitions along two 1-km long cables deployed horizontally across the ice surface within the node array. To our knowledge, this experiment is the first of its kind in Greenland. In the following, we present the experiment in detail, evaluate the seismic data quality and show preliminary results. We compare seismic power variations with variations in GNSS-derived surface velocity and other environmental parameters. We also build catalogs of seismic events, evaluate source location uncertainties, and demonstrate their relevance for seismic imaging.

2 Study area

We targeted the tongue of Isunnguata Sermia, a land-terminating outlet glacier on the western margin of the Greenland Ice Sheet, which is accessible on foot (Fig. 1). The glacier experiences strong seasonal summer surface ablation of approximately 4–6 m water equivalent (Van den Broeke et al., 2017). Previous borehole measurements, although mostly located higher up the catchment, have shown that the glacier is polythermal: ice temperatures range from -5 to -10 degrees within the first few hundreds of meters of depth, and increase to the pressure-melting point within a few tens to a hundred meters above the glacier bed (Harrington et al., 2015). The drilling campaigns also reported hard bed conditions, with limited to non-existent till at the ice-bed interface (Harper et al., 2017). Nevertheless, till is likely to be more prevalent within troughs, where drilling campaigns were limited due to greater ice thicknesses that make drilling more challenging. Constraints on glacier bed topography are provided by airborne radar (Jezek et al., 2013; Lindbäck et al., 2014), although there are fewer observational constraints over the glacier tongue due to higher signal attenuation and harsher ground survey conditions in this area.

In the targeted area, the existence of several subglacial lakes, each hundreds of meters in diameter, is suspected based on sudden surface subsidence and uplift events observed previously from the differencing of ArcticDEM digital elevation models (Livingstone et al., 2019). We targeted the region between subglacial Lakes 1 and 2 identified in Livingstone et al. (2019) (see black dashed lines in Fig. 1a–b), where ice thickness varies between 350–500 m and ice speed can reach up to 0.7 m/day in the summer (Jones et al., 2018), with several stations covering subglacial Lake 2, which is inferred to have drained in August 2015 and has supposedly refilled since then. Airborne radar reflectivity surveys upglacier have revealed persistent subglacial water storage on bedrock ridges in winter, which migrates to the subglacial troughs during the melt season (Chu et al., 2016). Thus, in summer and fall 2024, we extended the array northward to cover the large overdeepened bed trough (Lindbäck et al., 2014).

3 Deployment strategy and acquisition settings

3.1 Seismic Nodes

Our experiment was designed to study the evolution of seismic sources and glacier internal structure across multiple seasons to resolve the response to variations in hydrological conditions. Due to the challenging deployment environment and the limited 1-month autonomy of the sensors, we conducted three campaigns targeting three different times of the year: in spring 2023, near the onset of surface melt; in summer 2024, at maximum surface melt; and during fall 2024, at decreasing surface melt. In the following we describe the specifics of each campaign.

3.1.1 The 2023 campaign

The spring 2023 campaign targeted the time period from late April to the end of May. From April 25 to May 30, we deployed 82 Fairfield ZL 3C units with a sampling frequency of 250 Hz. These sensors have a lower cutoff frequency of 5 Hz, a sensitivity of 76.7 V/m/s (see Ringler et al., 2018, for a detailed laboratory analysis of sensor response characteristics), and a typical autonomy of about 35 days. Each unit comprises a sensor, a data logger, and a battery in a cylindrical casing with a diameter of 10 cm (Fig. 1f). We deployed the units $\sim$60 cm deep into a circular hole drilled with an auger 12.5 cm in diameter, providing a small clearance relative to the casing. The node deployment depth was chosen to ensure that the unit was deep enough to remain buried in the ice over the measurement period while being shallow enough for the GNSS signal to pass through the ice layer to ensure proper reception for time synchronization. The units were oriented toward geographic North using a compass, and a bamboo stick was inserted into each hole between the unit and the hole edge to help locate the nodes during recovery. The nodes were recovered between June 9 and June 13, 2023. The data availability from the spring 2023 deployment is shown in Figure S1.

3.1.2 The 2024 campaigns

The 2024 campaigns targeted the summer period from late June to the end of July and the fall period from early September to early October. 115 seismic nodes were deployed in similar locations during both of these time intervals over a study area of approximately 1.6 $\times$ 1.6 km^2 (Fig. 1b). The 2024 deployment extended further north than the 2023 deployment and did not include the southwest corner instrumented in 2023. This area is highly crevassed and, unlike in spring 2023 when the crevasses were filled with snow, the crevasses were largely open in 2024, making a repeated deployment too challenging. The 27 nodes originally planned to be deployed in the southwest corner were instead deployed as a dense sub-array of 0.3 $\times$ 0.3 km^2, located southwest of the French Ice Camp (FIC, Fig. 1b). The spatial distribution of nodes was defined following an aperiodic tile pattern geometry, which is expected to improve plane wave beamforming performance compared to regular orthogonal arrays (Mordret and Grushin, 2025).

Each node consisted of a Geospace GSB-3 recorder, which combines a data logger, and GNSS receiver for time synchronization, connected to a Geospace GS-ONE LF 5 Hz 3C geophone (Fig. 1g). The GSB-3 has 64 GB of onboard data storage and an internal battery life of up to 40 days. To extend this operating time, 12 additional external BN25 batteries were deployed, each capable of extending the autonomy of a GSB-3 recorder by approximately 200 days. All GSB-3 recorders were configured to record data with a 1000 Hz sampling rate, a 1 Hz low-cut filter, a linear phase alias filter, and a 24 dB gain.

Summer 2024

The installation procedure was designed to support both instrument protection and data quality, given the strong ice melt of 1–2 m water equivalent per month in summer. The nodes were deployed using a double-hole configuration drilled with a 15-cm-diameter auger. The deeper hole (0.8–0.9 m) and the shallower hole (0.1–0.15 m) accommodated the geophone and the GSB-3 recorder, respectively. The BN25 battery, when present, was placed directly on the surface. A custom-manufactured pole, able to clamp and release the geophone, was used to place the geophone at the bottom of the hole and orient it toward geographic North using a compass, correcting for the declination. Ice chippings were added around the geophone to stabilize its position and to enhance coupling with the surrounding ice. Two additional nodes were installed next to node 1058 to test the influence of the deployment protocol on data quality, specifically on tilt resilience, leading to a total of 117

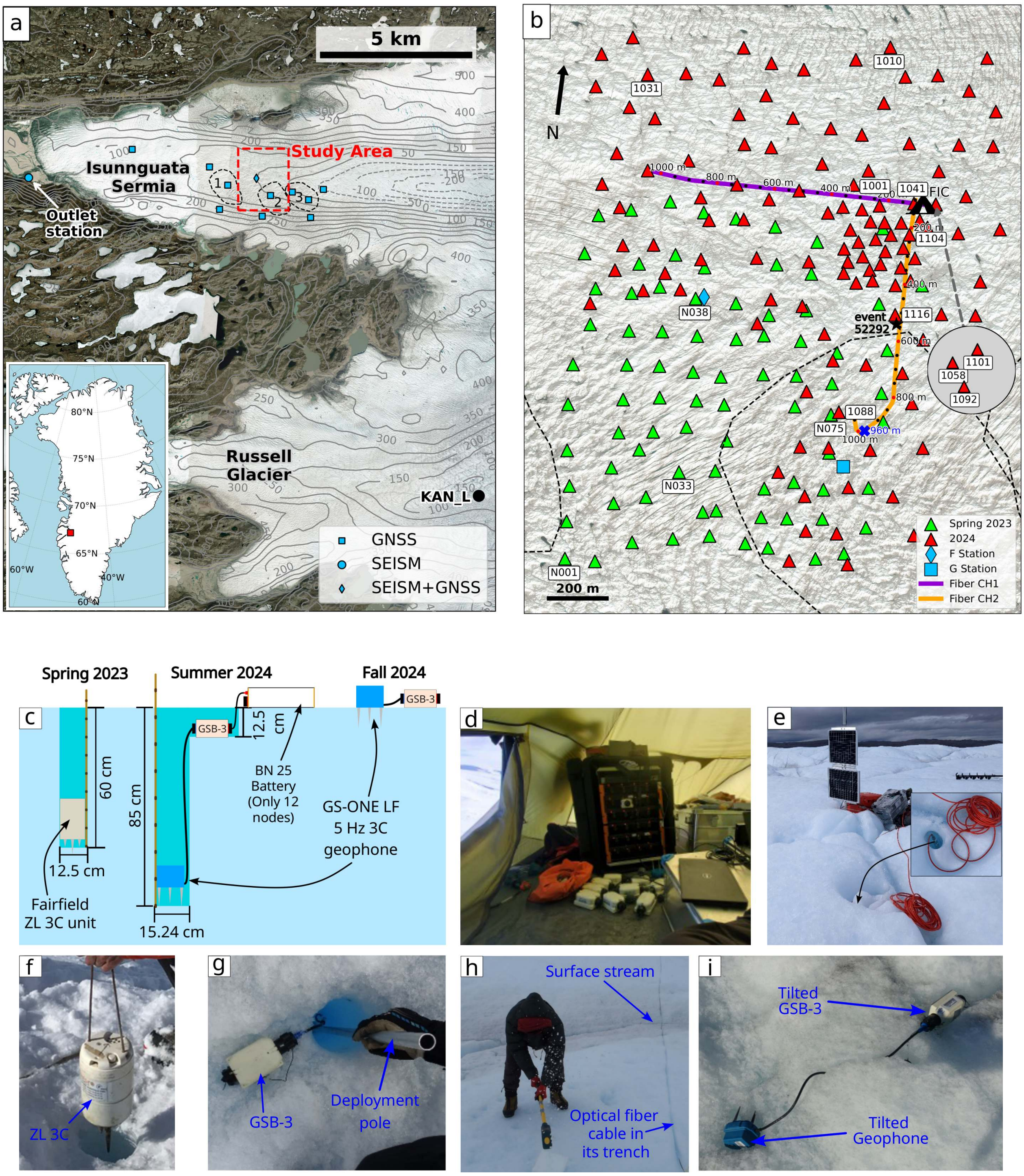

Figure 1 a) Bing satellite image of the region around the study area. The black dashed lines correspond to the outlines of subglacial lakes identified in Livingstone et al. (2019). The blue squares, circle, and diamond mark GNSS, seismic and GNSS+seismic stations, respectively. The gray lines show the bed elevation from BedMachine (Morlighem et al., 2017). The red dashed rectangle indicates the location of the study area in panel b). The red square in the inset indicates the location of the satellite image. b) Satellite image of the study area. Green and red triangles mark the 2023 and 2024 seismic nodes, respectively. The blue diamond and square indicate the locations of the GNSS F and G stations, respectively, with a long-term seismic station co-located at F. The purple and orange lines show the location of the optical fiber deployed in summer 2024 with the distance in the records. The dark blue cross on fiber CH2 shows the channel used in Figure 2j. The black star indicates the location of event 52292 shown in Figure 7. FIC marks the French Ice Camp location. c) Sketch of nodes deployment, as illustrated by the photographs f) and g). d) AYTOP portable GSB data transfer rack in the tent. e) F Station. h) Sledgehammer blow close to the optical fiber cable during the summer 2024 campaign. i) Tilted node 1052 observed during fall 2024.

nodes (Fig. 1b). The geophone of node 1101 was buried at the bottom of the hole with the battery placed on top of it. In contrast, node 1092 had its geophone, battery, and GSB-3 all deployed at the surface (Fig. S2a–c). The data availability from the summer 2024 deployment is shown in Figure S3.

Fall 2024

Seismic nodes from the summer were recovered; data were downloaded, and internal batteries were charged on site using the AYTOP portable GSB data transfer rack installed in a tent (Fig. 1d) and a power system as described in Section 3.4. This approach allowed the nodes to be re-deployed during the same field campaign. Visual inspection of the status of each sensor at recovery demonstrated that, despite being placed in boreholes, the sensors experienced significant tilt, and the surface geophone of node 1092 did not show greater tilt than the other two co-located nodes. Following these observations, we re-deployed all the sensors at the surface within 15 m of their summer 2024 location, with the exception of nodes 1101 and 1092 which were not re-deployed (Fig. 1c). The availability of the fall 2024 nodes data is shown in Figure S4.

3.2 Long-term seismic stations

In addition to the seismic node array, two long-term seismic stations were installed and maintained on the glacier and at its outlet in 2023 and 2024 (see Fig. S5 for a summary of data availability). A seismic station was installed at the glacier outlet, on the southern side of the valley on June 1, 2023 (Fig. 1a). The outlet seismic station was initially equipped with a Guralp Radian Posthole sensor sampling at 500 Hz and recorded by a Guralp Minimus logger. On August 28, 2023 a Digos DATA-CUBE^3 type 2 logger was installed alongside the Radian and set to record data at 100 Hz (https://digos.eu/the-seismic-data-recorder/) with a DiGOS 4.5 Hz 3-component geophone with a sensitivity of 28.0 V/m/s (https://digos.eu/geophone/) connected to a battery system powered by solar panels. The station stopped operating at the end of October 2023 due to insufficient power, as site constraints required the solar panels to face north. During the summer 2024 field campaign, the power system was replaced, the Guralp Radian Posthole was removed, the Digos DATA-CUBE^3 was successfully restarted, and it recorded continuously through fall 2024.

An on-ice seismic station was co-located with the GNSS F station on June 9, 2023 (Fig. 1b,e). It comprised a Type 2 DATA-CUBE^3 and a GEObit C100 borehole-type, 3-component, 50 mm diameter, 4.5 Hz geophone with a sensitivity of 1500 V/m/s (https://geobit-instruments.com/seismometers-seismic-sensors/c100_sensor_256/), installed 5 meters deep into the ice. The seismic station recorded data at a 400 Hz sampling rate from June 9, 2023 to August 14, 2023 and at 100 Hz from August 14, 2023 onward. The station was maintained on June 27, 2024, when the sensor was found to be tilted in the borehole and was re-deployed at 5 m depth. The seismic station was deployed using the same solar panel power system as that used for the GNSS stations (see Section 3.5.1). It acquired continuous data except for ~1.5 months data gap in January caused by limited sunlight. Both the outlet and F station remain operational and are recording data at present.

3.3 Distributed Acoustic Sensing

Two 1-km long optical fiber cables were deployed across the glacier as two orthogonal profiles (Fig. 1b). Profile 1 was ~965 m long and oriented east–west. Profile 2 was ~910 m long and oriented north–south, with two bends: one at 725 m (47° toward the west) and another at 876 m (119° toward the north). The starting point of both profiles was located near FIC, close to seismic node 1041. The installation of each 1-km fiber cable was completed in a single day by a three-person team. One person carried the fiber reel on their back, another guided the deployment using a handheld GNSS receiver, and the third ensured contact between the fiber and the ice using blocks of ice cut with a chainsaw. The location of the fiber cables was surveyed with Real-Time Kinematic (RTK) GNSS using a Leica GS10 receiver equipped with an AS10 antenna, which yields decimetric relative position uncertainties.

The coupling between the fiber cables and the glacier ice was a major source of concern on data quality. The dark optical fiber cable absorbed sunlight, causing localized melting of the surrounding ice and creating a shallow trench along approximately 80% of the cable. The remaining 20% of the cable length was either lying in surface streams (Fig. 1h) or suspended between surface irregularities.

DAS data were acquired with the FEBUS A1 DAS interrogator, which can interrogate two different optical fibers simultaneously. The interrogator was placed in a tent at FIC, where it remained connected to the fibers throughout the campaign. Both connected cables were LightMax Flatdrop, each containing two 1-km-long G657A2 single-mode tight fibers. We used a 1000 Hz sampling rate, 2 ms derivation time, 10 m gauge length, and 2 points per gauge length, leading to 4.8 m spatial sampling. These settings were chosen to balance spatial resolution, co-processing time, and data storage needs. DAS data were acquired over a period of 23 days in July 2024, 3 days in early September 2024, and 4 days in October 2024. The availability of the DAS data is shown in Figure S6.

3.4 Energy station for nodes and DAS infrastructures

A requirement for the summer 2024 deployments was to have sufficient available energy to charge all GSB-3 nodes on site (85.7 Wh per GSB-3) and run DAS acquisitions with a power consumption of ~200 W as continuously as possible. The electric power supply system installed at FIC consisted of multiple components designed for energy production, storage, and management. For electricity generation, the setup included a gasoline-operated generator with a maximum output of 2 kW, and a 6-liter fuel tank, which results in an autonomy of 4–8 hours. Solar power was harnessed using three separate clusters of 55 W and 60 W photovoltaic panels, providing a total of 460 W. For energy storage, the system used eight 12 V batteries arranged in four

24-V banks. Two of these banks consisted of 90-Ah batteries and the other two of 100 Ah batteries, thus providing a theoretical total of 760 Ah at 12 V, or 9120 Wh. To manage the power flow and deliver clean 220 V AC, a 24 V–1600 W Victron Multiplus inverter and Victron SmartSolar MPPT 75V-15AS were used. The multiplus received the AC input from the generator while the MPPT received the DC input from the solar panels to charge the batteries while providing power to the camp and devices such as the DAS, data transfer rack, and laptops. A Victron Cerbo GX device monitored and recorded all aspects of the power system, including generator and solar panel production, battery charge levels, and instantaneous power consumption. The power supply system was sufficient to fully charge all GSB-3 recorders during fall 2024. While the GSB-3 recorders were charging, the data acquired since the summer 2024 deployment were downloaded, and their memory was cleared before being deployed again. The multi-day to multi-week DAS acquisitions were made possible by an on-site team that refueled and restarted the generator every two to three days.

3.5 Supporting datasets

3.5.1 GNSS measurements of ice surface motion

Time series of horizontal and vertical ice surface motion were determined from dual-frequency (L1 + L2) Global Navigation Satellite System (GNSS) data recorded by Leica GS10 (Site F) and GM30 (Site G) receivers at 0.1 Hz. GNSS stations G and F were deployed at the center, and to the northeast, of previously-identified Subglacial Lake 2 respectively (Fig. 1a). GNSS antennas were mounted on a 6-m-long aluminium pole drilled 5 m into the ice surface. Rapid re-freezing of the hole secured the antenna pole within the ice. The stations were powered by two 50 W photovoltaic panels connected to a battery bank of two (Site F) or four (Site G) 80 Ah lead acid batteries, which allowed them to operate almost continuously over one year, with only a brief interruption of a few months around January due to a lack of solar input. Data were post-processed kinematically (King, 2004) relative to a bedrock-mounted reference station using the differential carrier-phase positioning software Track v1.53 (Chen, 1998). Baseline lengths were < 3.0 km and precise ephemerides from the International GNSS Service were used (Dow et al., 2009). Positioning uncertainties were estimated at $\sim$0.01 m in the horizontal and $\sim$0.02 m in the vertical by calculating the standard deviation of the residuals from linear regression applied to the position time series during a month-long period of steady ice motion in November 2023. Small (< 5 min) gaps in the position record were linearly interpolated before a second-order 6 h low-pass Butterworth filter was applied. The position record was then resampled to 10 minute medians and differentiated to calculate velocity, which was further filtered using a 6 h moving average. To prevent phase shifts, phase preserving filters, differentiation, and resampling methods were used throughout.

3.5.2 Meteorological data

Surface melt over Isunnguata Sermia was modeled using COSIPY, a coupled snow pack and ice surface energy and mass balance model in Python (Sauter et al., 2020). This model was forced by data (shortwave radiation, air temperature, relative humidity, air pressure, wind speed, all-phase precipitation, and cloud cover fraction) from the Programme for Monitoring of the Greenland Ice Sheet - Greenland Climate Network (PROMICE - GC-NET) KAN_L weather station (Fausto et al., 2021) situated 12 km southeast of the seismic array. Air temperature from KAN_L was extrapolated over the Isunnguata Sermia margin using elevation from the Arctic DEM and a constant lapse rate of -5.3 °C/km (Harper et al., 2011). Atmospheric pressure was corrected using barometric equation. Precipitation for the COSIPY model was extracted from the nearest grid point of the ERA5 Land reanalysis model (Muñoz-Sabater et al., 2021).

4 Data quality control

4.1 Nodes and DAS Power Spectra

Both the seismic nodes and the DAS operated in highly dynamic glacial conditions, where melting and ice ablation can affect the coupling between the ice and the sensors. During the retrieval of the spring 2023 nodes, no tilt was observed, likely because surface melting was minimal during this period and the sensors remained well embedded in the ice. In contrast, during the summer 2024 deployment, the drilled holes remained filled with water. Melting likely increased later in the season as sensors became exposed at the surface, allowing them to tilt. This is consistent with the tilt observed for multiple sensors in fall 2024 (Fig. 1i). Meanwhile, melt around fiber cables and surface streams (Fig. 1h) impacted the coupling with the ice. To investigate the impact of these mechanisms on the quality of the signal recorded by the seismic nodes and DAS, we compute their time-dependent Power Spectral Density (PSD) using the Welch method with 10 s windows and 50% overlap applied to 1-h data segments.

4.1.1 PSD of Node records

In the nodes PSD (Fig. 2a–i), we observe strong transient power decreases below 20 Hz on all sensor components, particularly in summer 2024 (hashed areas in Fig. 2b,e,h). These power drops occur when the geophone tilt exceeds 30°, 8°, and 8° for the vertical, north, and east components, respectively, causing the coil to hit the end stop. Notably, seismic power often returned to pre-anomaly levels after these episodes, suggesting that the geophones were able to passively re-level without manual intervention.

We compare the data from the three co-located nodes deployed in summer 2024 to test the impact of the deployment on sensor tilt. On July 4, 2024, we noticed that the geophone of the surface-only protocol test node 1092 was significantly tilted in the N-S direction (Fig. S2c); hence, it was re-deployed. This N-S tilt by July 4 and the re-deployment can clearly be identified in the

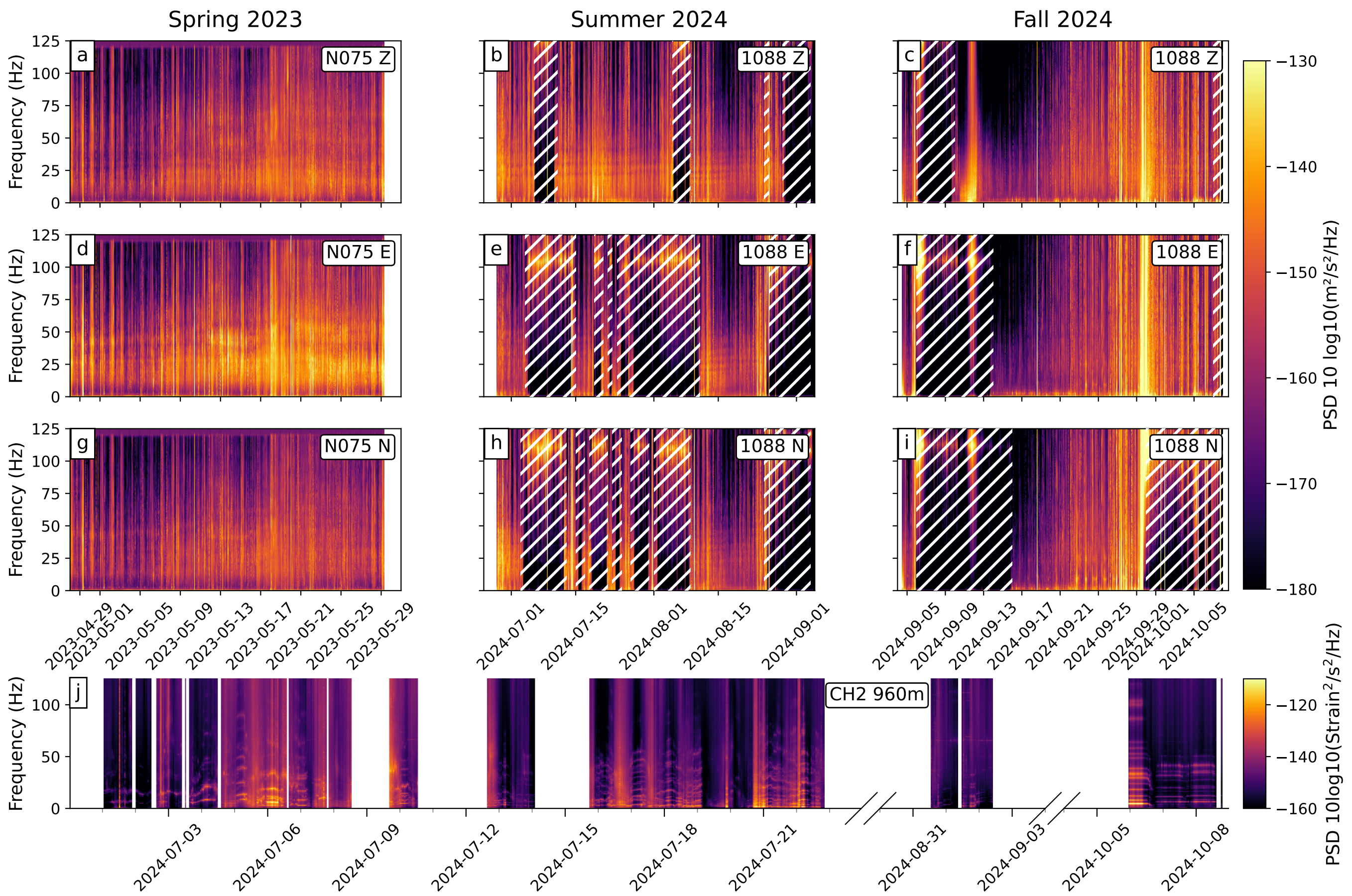

Figure 2 Power Spectral Densities (PSDs) of seismic nodes recordings for spring 2023 (a,d,g), summer 2024 (b,e,h) and fall 2024 (c,f,i). The top right inset indicates the name of the node and the component. The locations of node N075 and node 1088 are shown in Figure 1b. The hashed areas highlight days when the sensors were classified as significantly tilted (30° and 8° for vertical and horizontal components). j) PSD of the DAS channel CH2 recordings at 960 m along the fiber cable (see location in Figure 1b).

PSD associated (Fig. S2k). PSD analysis reveals that this node started to tilt again two weeks later in the E-W direction (Fig. S2l). During the same time period, the geophone in the hole (node 1058) tilted briefly in the N-S direction (Fig. S2e) and tilted multiple times in the E-W direction (Fig. S2f). Although the surface and buried geophones (nodes 1092 and 1058) both tilted in the N-S and/or E-W direction, their tilt did not exceed 30°, as their vertical component PSD does not show any spurious power drop (Fig. S2d,g). In contrast, the PSD of the geophone buried in the hole with a battery on top (node 1101) indicates long periods of tilt in both directions (Fig. S2h–i), which were temporarily greater than 30° (Fig. S2). This large tilt may be due to the battery pushing the geophone downward. Overall, the surface geophone (node 1092) performed as well, if not better, than the buried geophones (nodes 1058 and 1101), as it experienced shorter tilted periods. It may thus not be worthwhile to place geophones into holes unless they fit tightly, as was the case in 2023 with the 10-cm-diameter Fairfield nodes installed in a 12.5-cm-diameter hole.

To identify and remove data strongly affected by tilt, we generate catalogs of days with significant geophone tilt using a threshold on the PSD within the 5–20 Hz band. In the 2023 dataset, 100% of vertical and 98% of horizontal records were acquired with sensors operating within their tilt limits. In contrast, the summer 2024 dataset shows a decline in data quality, with only 80% of vertical records and 36% of horizontal records below the tilt limit. The fall 2024 dataset exhibits some improvement, with 92% of vertical and 55% of horizontal records below the tilt limit. In subsequent analyses, data from strongly tilted stations are systematically discarded.

4.1.2 PSD of DAS records

We computed the PSD of channel 960 m on fiber CH2 (Fig. 1b), which records E–W and N–S strain rates due to the bend in the profile. The seismic power on the DAS record shows strong similarities to the node. Most of the seismic power is concentrated below 50 Hz, but it exhibits narrower high-amplitude spectral lines (Fig. 2j). The frequencies of these spectral lines vary over time during summer but remain stable in October. Similarly to the nodes, the DAS records also show abrupt and large changes in seismic power, for example on July 4 and July 19. These variations may be spurious and could, for instance, result from changes in the coupling between the fiber and the ice. Identifying the mechanisms responsible for the observed spectral lines, as well as the origin of these abrupt variations in seismic power, is left for future investigation.

4.2 Active seismic measurements

We generated controlled seismic sources through series of ∼10 sledgehammer blows performed 5 m away from 95 of the deployed nodes. In each series, we hit a plastic plate lying on the ice surface with a ∼6 kg sledgehammer every ∼10 s. Figure 3a shows a section from a single sledgehammer blow next to node 1104 (Fig. 1b) recorded by seismic nodes in the vertical component, filtered between 100–200 Hz. A Rayleigh wave with a velocity of ∼1650 m/s is clearly observed over hundreds of meters from the source. A P wave with a velocity of ∼3750 m/s can also be discerned, although with a much weaker signal. Figure 3b shows the same event recorded by the DAS system, filtered in the same frequency band as Figure 3a. The seismic waves generated by the blow are also detectable on the DAS; however, they are only observable within approximately 25 m of the source. This significant difference can be explained by multiple effects, such as poor coupling of the DAS cable, the difference in the directionality of the signal (vertical/horizontal), and the source-station direction, as the source was offset by a few meters from the fiber cable.

We compare the waveforms recorded by node 1104 with those recorded by the closest DAS channel during this sledgehammer blow (Fig. 3c). We select the North component of the node, collinear to the direction of the N-S fiber (CH2), deconvolve its instrument response, and convert the strain rate recorded by the DAS to velocity with a spatial integration followed by sliding mean removal (Trabattoni et al., 2023) so that both measurements can be compared. We find that the waveforms have a similar envelope, with a clear large-amplitude transient followed by a short coda. However, the noise level is significantly larger on the DAS compared to the node.

A comparison of sledgehammer-blow waveforms recorded by DAS and collocated seismic nodes reveals significant time desynchronization between them. For example, node 1097 records exhibit a constant lag of approximately 0.46 s relative to DAS records at the time of the blows (Fig. S7a). Such time desynchronizations compromise seismic node array analysis and comparison with DAS.

4.3 Clock synchronization assessment and correction

We systematically evaluate the clock synchronization of the seismic nodes throughout all three deployment campaigns. To assess node clock stability, we compute hourly ambient noise correlation functions (details on calculation in Section S1 of the Supplementary Material), which approximate the Green's function between station pairs (Campillo and Paul, 2003), and filter them between 10–20 Hz. The time drift caused by GNSS desynchronization at one station produces an asymmetric shift between the causal and anticausal parts of the correlation function, which we use to resynchronize the sensor (Stehly et al., 2007).

During the spring 2023 campaign, correlograms exhibit overall stable noise correlations, and only few station pairs are affected by clear drifts indicative of time desynchronization caused by GNSS signal loss. For example, the correlogram of pair N001–N033 (Fig. 4a) exhibits a linear drift beginning on May 23, 2023 (green shading), with a rate of several tens of milliseconds of desynchronization per day. Importantly, this drift begins several days after station N033 lost GNSS synchronization, as indicated by the Fairfield ZL logs (green line in Fig. 4a). This highlights the need for a careful selection of the time windows used to estimate and correct for clock drift.

We observe similar clock-desynchronization periods with the Geospace GSB-3 recorders in summer 2024, whereas none are detected in the fall 2024 dataset. Unlike in 2023, desynchronization occurs immediately after GNSS loss in summer 2024 and often persists until the day following re-synchronization. For example, node 1010 was logged as re-synchronized on July 25, 2024, but the re-synchronization only took effect on July 26, when the drift coefficient changed abruptly in the pair 1001-1010 correlogram (Fig. 4c). We observe a singular case for node 1097, which, despite continuously receiving the GNSS signal, shows a continuous drift throughout the summer 2024 deployment (Fig. S7b). Additionally, the 2024 desynchronizations induce not only drift but also variable time offsets that differ between nodes and across episodes (Fig. 4c).

We manually identify all affected stations and estimate their offsets and drift rates for the spring 2023 (Fig. 4b) and summer 2024 (Fig. 4d) campaigns (details on clock correction in Section S2 of the Supplementary Material). Although DAS records are correctly synchronized in time at the beginning of the deployment, recorded logs reveal GNSS signal losses at later times (Fig. S6). A systematic quantification and correction of the time desynchronization of the DAS records is required before this data is integrated with node records.

5 Preliminary results

5.1 Spectral signatures of seismic sources and links with water input and glacier dynamics

We show in Figure 5a the PSD of the seismic signal recorded at F station over the 2023 and 2024 periods of interest, supplemented by the PSD of node N038 (Fig. 1b) collected prior to the deployment of the F station. We observe strong variations in seismic power occurring over a range of frequencies and temporal scales. Seismic power exhibits a clear seasonal pattern, increasing during summer as air temperatures rise and surface melt rates increase. This seasonal change is accompanied by a shift in frequency content: in spring 2023, seismic energy is primarily concentrated above 5 Hz, whereas during the summer of 2024 it extends to lower frequencies, down to 1 Hz. In addition to this long-term trend, seismic power shows high amplitude broadband peaks associated with rainfall events, such as the one in late September, which could result from

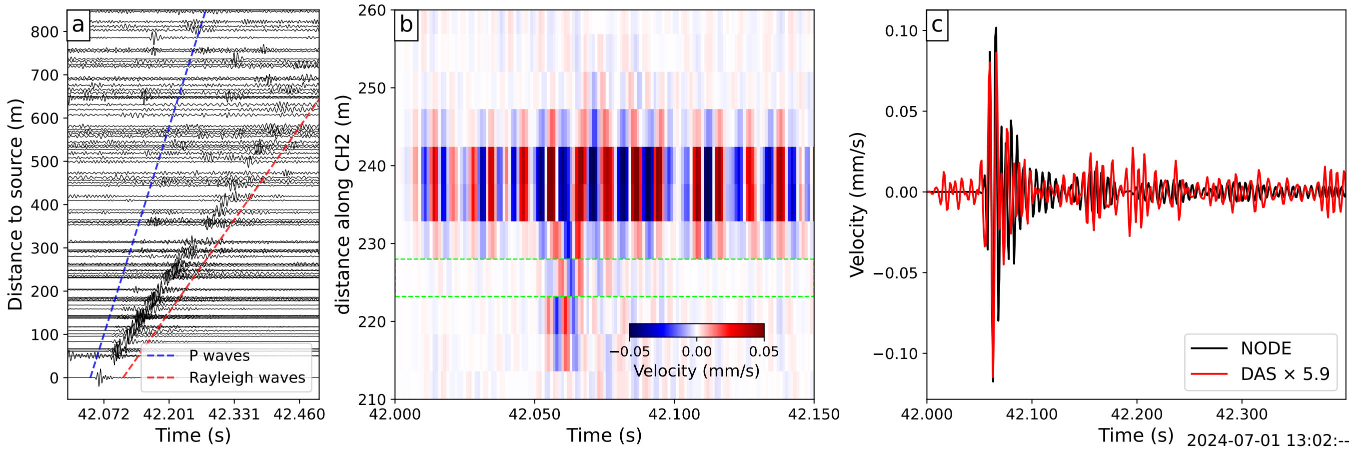

Figure 3 a) Vertical component shot gather of a sledgehammer blow close to node 1104 (Fig. 1b). b) DAS section converted to velocity for the same event. The light green box shows the channel closest to node 1104. c) Comparison between the waveforms of the North component of node 1104 and that of the DAS channel in the light green box in panel b). All waveforms are filtered in the 100–200 Hz range.

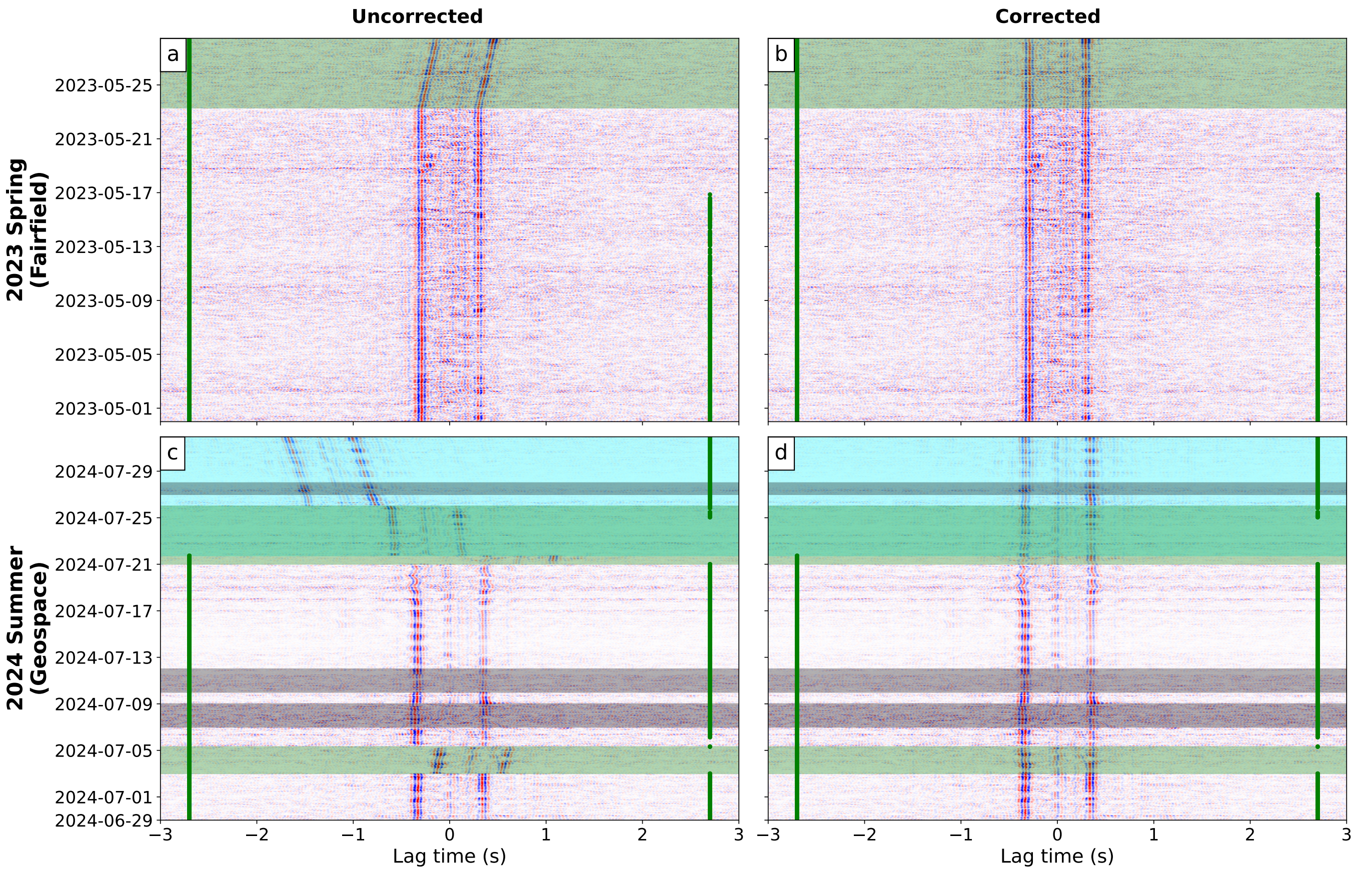

Figure 4 a–b) Correlogram between the vertical component of 2023 nodes N001 and N033 filtered between 10–20 Hz, a) before and b) after time resynchronization. c–d) Same as a) and b) for 2024 nodes 1001 and 1010. Cyan and green shaded areas indicate the time where we manually identified a clock desynchronization for the first and second station of the correlation pair, respectively. The green dots indicate when nodes received GNSS signal. The gray shaded areas indicate days when at least one of the two stations of the pair is significantly tilted.

the short-term increase in glacier velocity possibly enhanced by rain-induced sliding (Horgan et al., 2015). Superimposed on the seasonal trend is a distinct diurnal signal well correlated with temperature (Fig. 5c). This can be observed during periods of minimal precipitation and surface melt (e.g., from April 28 to May 3, 2023), when large diurnal temperature fluctuations coincide with clear diurnal variations in high-frequency seismic power. Interestingly, seismic power averaged in the 4–6 Hz band, dominated by subglacial water-flow-induced seismic noise (Bartholomaus et al., 2015; Gimbert et al., 2016; Nanni et al., 2021), correlates well with glacier surface velocity variations measured by GNSS (Fig. 5b). Large peaks in glacier surface velocity are generally associated with large increases in seismic power, with a few exceptions, such as on July 26, 2024, when a peak in GNSS velocity is not associated with a peak in seismic power, or on September 4, 2024, when a peak in seismic power is not associated with a significant increase in glacier surface velocity (Fig. 5b,c).

5.2 Analysis of the ambient noise wavefield from noise correlation functions

In Figure 6a,c,d, we show stacked hourly noise correlation functions filtered at high-frequency (40–80 Hz) and sorted by inter-station distance for spring 2023, summer 2024, and fall 2024, respectively. Even at these high frequencies, the vertical-vertical (ZZ) component of the spring 2023 data reveals clear P- and Rayleigh-wave arrivals, which are symmetric at negative and positive lag times and persist up to inter-station distances of 900 m and 1200 m, respectively (Fig. 6a). In summer 2024, the strong increase in noise power around 0-s lag time significantly reduces the signal-to-noise ratio (SNR) of Rayleigh waves, and P waves are no longer visible (Fig. 6c). In fall 2024 the noise level decreases relative to the summer, and both P and Rayleigh waves reappear, though with a lower SNR than in spring 2023 (Fig. 6d). Despite the lower SNR, we reconstruct the fall 2024 P and Rayleigh waves over greater inter-station distances than in 2023, which results from the increased number of available station pairs with large inter-station distances (blue curve in Fig. 6a–d). In the transverse-transverse (TT) component, we also observe clear Love waves in the 10–20 Hz range (Fig. 6b).

Surface melt appears to strongly influence noise correlation functions. We observe large amplitudes around 0-s lag time in summer 2024, when surface melt rates are high; moderate amplitudes in fall 2024, when melt rates are low; and small amplitudes in spring 2023, when there is little to no surface melt (Fig. 6a,c–d). Several surface streams cross the array and generate significant seismic energy; as a result, the generated seismic waves reach both stations at a similar time, producing spurious arrivals centered at 0-s in the noise correlation functions. Part of these spurious arrivals can also arise from the near-vertical incidence of waves generated by deep englacial or subglacial hydrological sources.

We used these correlation functions to calculate the frequency–velocity diagram averaged across the array, using the slant-stack method of Park et al. (2005), which estimates signal power as a function of phase velocity by applying offset-dependent phase shifts. Across the different recording periods, the P and Rayleigh wave velocities remain constant above 20 Hz (Fig. 6e–g). Below 20 Hz, Rayleigh wave phase velocity slowly decreases alongside frequency in 2024. In spring 2023, we observe a steep ∼150 m/s change in the Rayleigh wave phase velocity around 10 Hz (Fig. 6e), which is not observed in 2024 (Fig. 6f–g). The origin of this sharp velocity change remains uncertain, and the discrepancy between 2023 and 2024 could be due either to a temporal change in the medium or to spatial variations, because the 2023 and 2024 arrays do not cover the same area. Below 3 Hz, where Rayleigh waves are mostly sensitive to depths greater than 200 m, the phase velocity slowly starts to increase as the frequency decreases. This increase in velocity with decreasing frequency (increasing depth sensitivity) may reflect higher S-wave velocities in deeper ice, or sensitivity to a high-velocity bed beneath parts of the array where the ice is the thinnest (∼350 m in the southwestern corner). Below 2 Hz, the dispersion curve of Rayleigh waves is no longer properly resolved due to the limited aperture of the array (black dashed line in Figure 6e–g).

5.3 Seismic event detection and localization with Matched Field Processing

We use Matched Field Processing (MFP) (Baggeroer et al., 1988; Chmiel et al., 2019; Gimbert et al., 2021) in the 4–6 Hz frequency band to locate seismic events and construct seismic event catalogs for the 2023 and 2024 datasets. MFP evaluates the mismatch between the phases recorded by all stations across the array and those predicted for a hypothetical seismic point source defined by its three-dimensional location and wave phase velocity. The degree of phase coherence is quantified using the normalized Bartlett output (BO) which ranges from 0 to 1. BO values close to 1 indicate a good match between observed and synthetic phases. We employ the Nelder–Mead algorithm (Nelder and Mead, 1965), a derivative-free local optimization method, to optimize the source coordinates and phase velocity that maximize the BO. In Section S3 of the Supplementary Material, we provide more details on the MFP parameterization and our strategy for designing the source location optimization for events with optimal BO > 0.3. In the following subsections, we report well-located events associated with BO > 0.3.

5.3.1 An example of a natural event as recorded with Nodes and DAS

Due to the uncertain coupling of the optical fiber cable under surface melt, we assess the quality of the DAS data by comparing its signals with those from seismic nodes during a natural event from the MFP catalog (Fig. 7). For this comparison, we chose the summer 2024 event 52292 (Fig. 1b), which occurred on July 17, 2024, at approximately 22:23:40.6 UTC (22:23:40-42 MFP time window) during a period of high surface melt (Figure 5c). This event is associated with a high BO (BO > 0.9) and is close to node 1116, which is located near the fiber cable CH2. This event can be observed in the records of all non-tilted nodes of the summer 2024 array, as it generates high-amplitude Rayleigh waves (Fig. 7a). The P waves generated by the event can be observed up to ∼600 m from the source. At the time of the event, some stations were significantly tilted (red and purple waveforms in Fig. 7a). These stations recorded a significantly higher frequency signal than non-tilted stations, effectively filtering out surface waves far from the source. Multiple nodes were also desynchronized at the time of the event (dashed blue waveforms in Fig. 7a). For instance, node 1031 (Fig. 1b) was desynchronized for ∼32 hours by the time of the event (Fig. S3), which resulted in arrivals too early by ∼0.5 s. After correcting

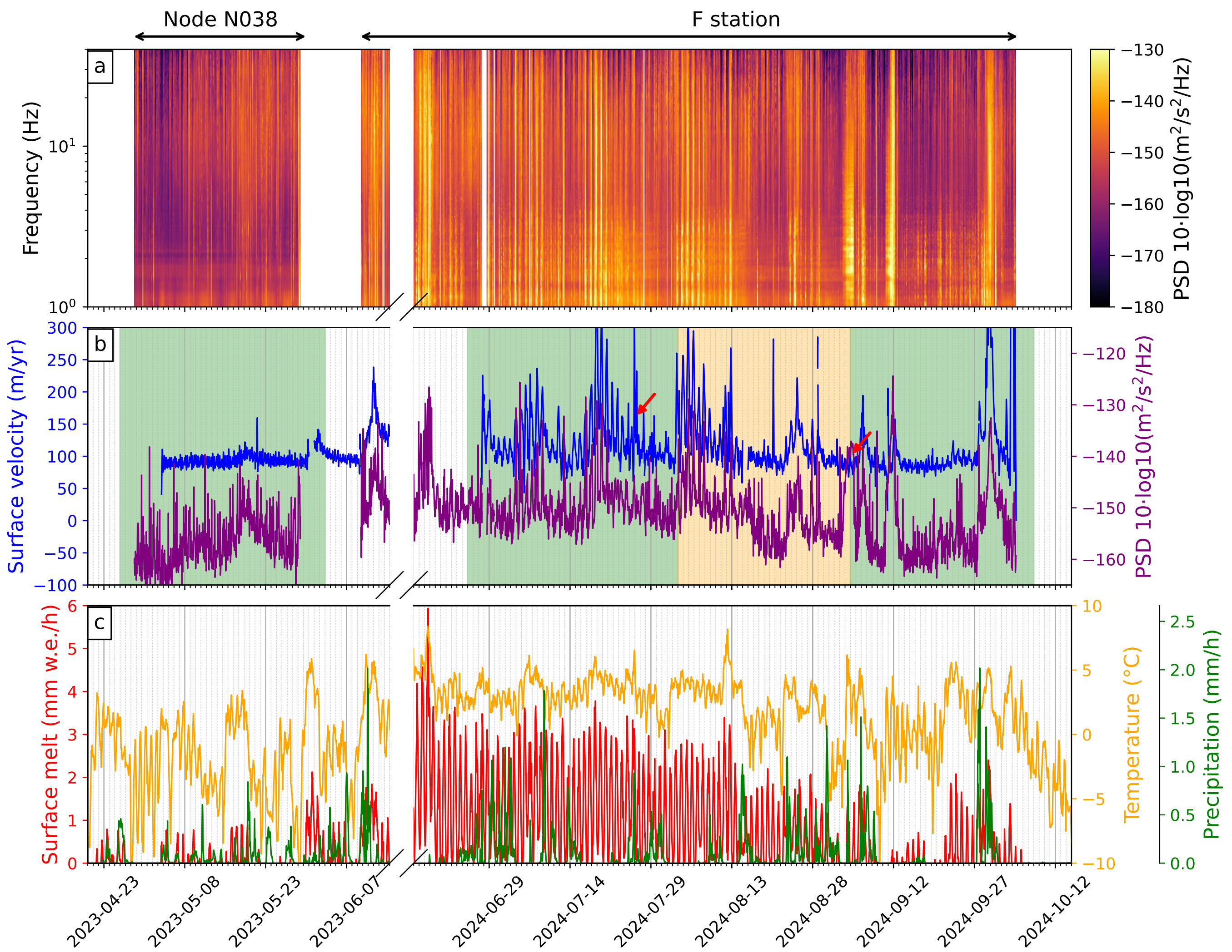

Figure 5 a) Power spectral density of node N038 and F station. b) Comparison between a) averaged in the 4–6 Hz frequency band (purple) and surface velocity derived from the GNSS F station (blue). The red arrows indicate examples of days where the noise power and surface velocity do not peak at the same time. The green and orange shaded areas indicate periods when the seismic arrays were deployed with most nodes and a limited number of nodes, respectively. c) Meteorological parameters at F station. The orange, green and red lines represent the surface temperature interpolated from KAN_L on the ArcticDEM grid, precipitations from the nearest ERA5 Land reanalysis grid cell and modeled surface melt with COSIPY (Sauter et al., 2020), respectively.

for this delay, the waveforms align well with records at the other nodes (solid blue waveforms in Fig. 7a).

In the records of the DAS CH2 cable, Rayleigh wave propagation can be observed up to hundreds of meters from the source (Fig. 7b). However, surface wave arrivals are masked where the fiber cable crosses surface streams because of the noise that dominates the signal. Note that this seismic event was observed from 22:23:39.6 in the DAS records, ∼1 second before the estimated origin time, which indicates significant time desynchronization of the DAS system when the GNSS signal is lost.

In Figure 7c, we compare the waveforms recorded by the north component of node 1116 and its closest DAS channel. The DAS waveform was time corrected and converted from strain rate to velocity, while the node waveform was corrected for the instrument response and converted to velocity. Both waveforms were filtered between 20–50 Hz. The DAS waveform is similar to the node recording, but the node has a significantly higher SNR.

We compute the frequency–velocity diagram from the 50 to 500 surface events with BO > 0.9 in the different datasets, using the MFP algorithm without averaging BO over frequency (Fig. 7d–f). These diagrams are similar to the results obtained from ambient noise correlation functions. The BO value is maximized for frequency and velocity values similar to the power in Figure 6e–g. Above 40 Hz, P waves with velocities around 3750 m/s dominate, whereas below 40 Hz, Rayleigh waves dominate. The Rayleigh waves have a constant phase velocity of ∼1650 m/s between 20–40 Hz. The abrupt Rayleigh wave velocity discontinuity observed around 10 Hz in 2023 (Fig. 7d) is consistent with that observed from the noise correlation frequency-velocity diagram (Fig. 6e), although it is less pronounced, likely due to differences in spatial coverage. In 2024, additional smaller but steep velocity changes appear between 20 Hz and 25 Hz

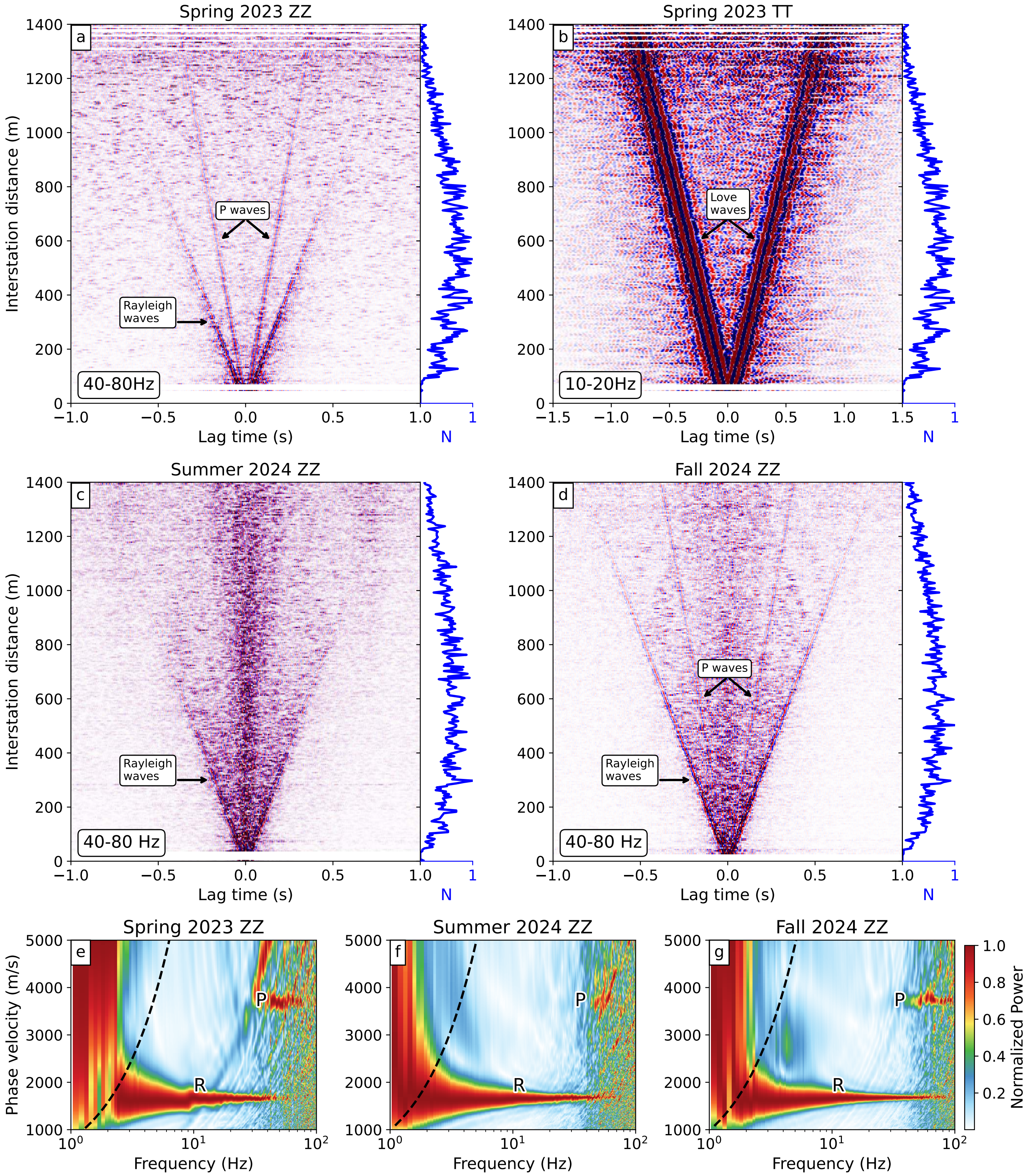

Figure 6 Spring 2023 time averaged vertical-vertical (ZZ) a) and Transverse-Transverse (TT) b) noise correlations filtered between 40–80 Hz and 10–20 Hz, respectively. c–d) Time averaged ZZ noise correlations for summer 2024 and fall 2024. The blue curves in a-d indicate the normalized number of correlation functions stacked in each interstation distance bin. e–g) Frequency-velocity diagrams for the ZZ components of spring 2023 e), summer 2024 f) and fall 2024 g). The black dashed line indicates the frequency-dependent resolution limit, given the maximum wavelength and sensor spacing $\lambda_{max} = \Delta_{max}/2$. "P" and "R" indicate P and Rayleigh waves.

(Fig. 7e–f), which were not resolved by the frequency-velocity diagrams from noise correlation functions (Fig. 6f–g). Furthermore, P waves are significantly clearer in the event frequency-velocity diagrams and remain well above the noise level during summer 2024 (Fig. 7e). The strong similarity between the noise-based and event-based frequency–velocity diagrams supports the reliability of our MFP analysis and optimized source locations.

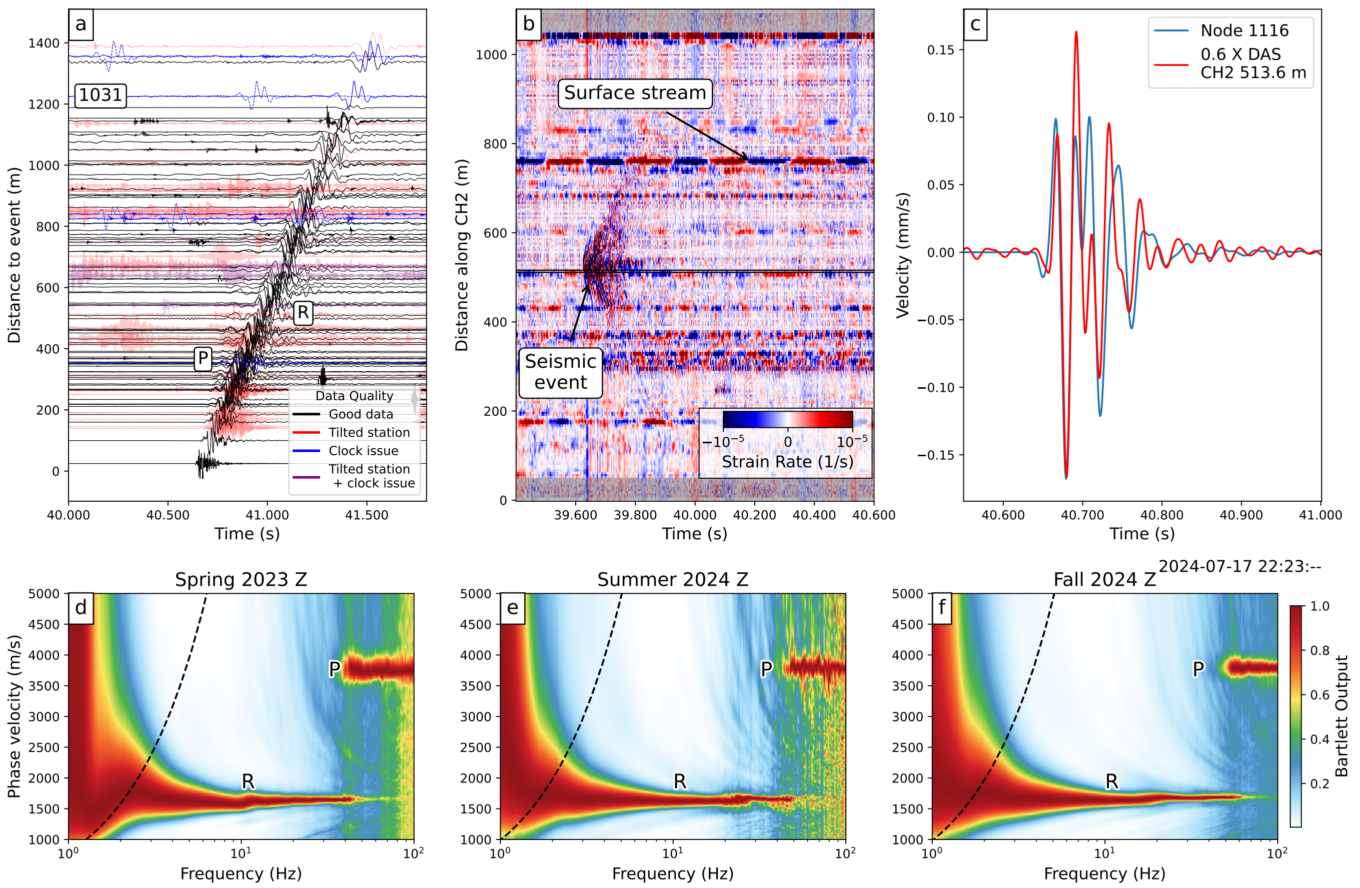

Figure 7 a) Nodes vertical component waveforms recorded during event 52292 in summer 2024 (location in Fig. 1b). P and R indicate the direct P and Rayleigh wave arrivals. The color of the waveforms indicates the status of the station as indicated in the legend. The dashed waveforms show the data before clock correction. b) DAS record along fiber CH2 for the same event. The 0–50 m and 1050–1100 m gray-shaded region indicate where no optical fiber is present. The thin black box indicates the channel used in panel c). c) Comparison between the signals recorded by the north component of node 1116 and its closest DAS channel in the 20–50 Hz band. d–f) Frequency-velocity diagrams from surface BO > 0.9 events in d) spring 2023, e) summer 2024, and f) fall 2024. The black dashed line indicates the frequency-dependent resolution limit, given the maximum wavelength and sensor spacing $\lambda_{max} = \Delta_{max}/2$. "P" and "R" indicate P and Rayleigh waves.

5.3.2 Spatial distribution of natural events

During spring 2023, BO > 0.8 events, hereafter referred to as high Bartlett output (HBO) events, occur predominantly near the surface and closely match the pattern of surface crevasses, suggesting that these are crevassing events (Fig. 8a). Two regions exhibit deeper events in 2023; the center-southeast region and the northwest region, with 100–200 m and 200–300 m deep events, respectively. In summer 2024, the MFP localized fewer HBO sources overall, with only sparse detections in the southwest crevasse field and very few sources in the northwest. Moreover, the spatial distribution of these sources shows limited alignment with surface crevasses (Fig. 8b). The fall 2024 results exhibit an intermediate pattern between spring 2023 and summer 2024: more seismic sources are detected than in summer, particularly in the central region, where they align more clearly with surface crevasses (Fig. 8c).

Overall, there is a clear change in the event depth distribution from 2023 to 2024, as the fraction of surface events drops from 40% in spring 2023 to $\sim$20% in 2024 (Fig. 8d,f,h). This change in source depth is also accompanied by a decrease in the proportion of HBO events in summer 2024, where the cumulative proportion of HBO events decreases from $\sim$13.8% to $\sim$7.1% between spring 2023 and summer 2024 (Fig. 8e,g). The proportion of HBO events in fall 2024 increases back to $\sim$11.5%, but the depth distribution of fall 2024 events remains similar to that of summer 2024 (Fig. 8i).

In the following, we investigate the uncertainty in the locations of these seismic events and the origin of discrepancies in the BO between different periods, to verify that the observed changes are physical rather than artifacts arising from varying configurations.

5.3.3 Uncertainties of MFP-derived source locations

We assess the uncertainties of MFP-derived source locations by generating synthetic events with waveforms at a central frequency of 5 Hz to which we add background noise. We evaluate the uncertainty on synthetic events with different optimal BO values by modulating the background noise power (see Section S4 of Supplementary Material for technical details). For each synthetic event, we measure the horizontal and vertical distances between the optimized and reference source lo-

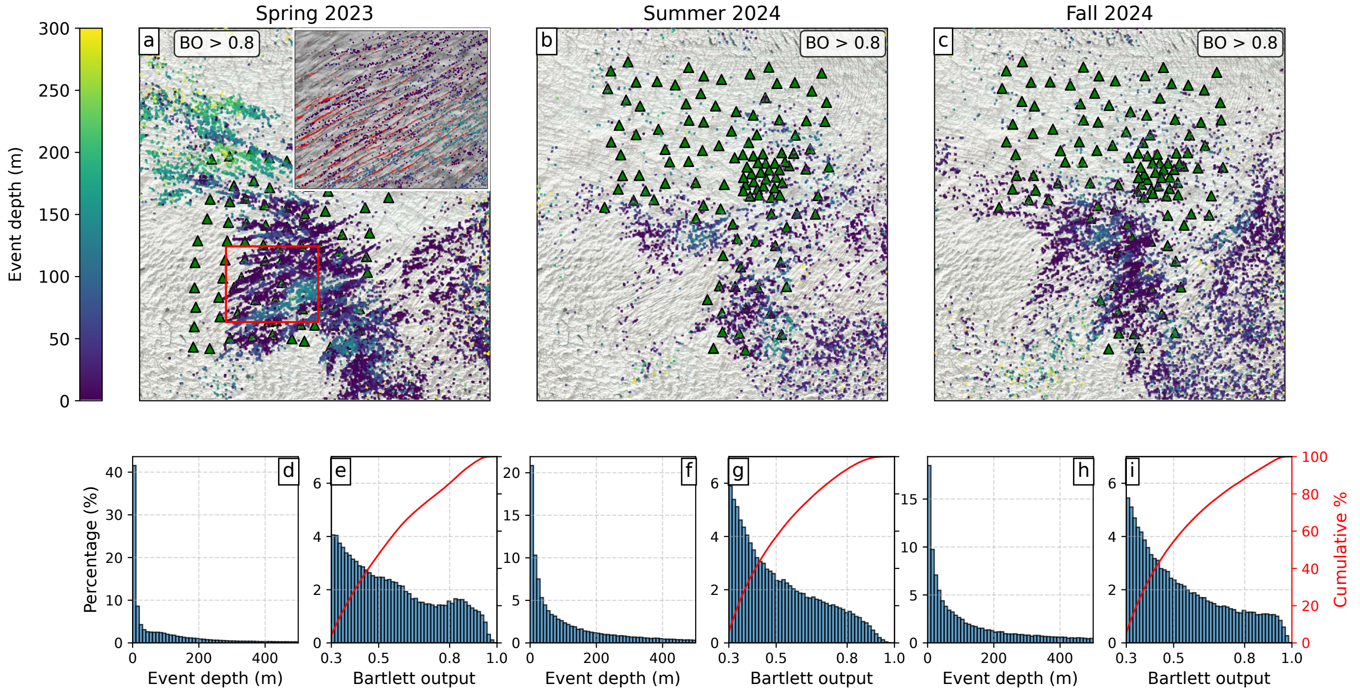

Figure 8 Map of MFP-based high Bartlett output (HBO) event locations in a) spring 2023, b) summer 2024 and c) fall 2024. The green triangles show the location of the seismic nodes used for the MFP analysis. The colormap shows event depth. The inset in a) shows a zoom in the red rectangle. The red lines in the inset highlight the surface crevasses extracted from the July 2023 Pleiades background satellite image. d)–i) Histograms of event depth and Bartlett output for the three acquisition periods.

cations, which we refer to as horizontal resolution (h_{err}) and vertical resolution ($|z_{err}|$). Figure 9 shows the resolution estimated on a grid of events. At the first order, the resolution depends on the optimum BO value and the location of the event with respect to the array.

Inside the array, surface events (0 m depth) with a very high BO (BO > 0.9) have a vertical resolution of 7 m and 10 m, for the 2023 and 2024 arrays, respectively (Fig. 9b,d,f), while the horizontal resolution is 1 m for all arrays (Fig. 9h,j,l). For low BO (0.3 < BO < 0.4) events, the vertical resolution of surface events inside the array decreases to 16 m and 20 m in 2023 and 2024 (Fig. 9a,c,e), respectively, while the horizontal resolution decreases to 5 m for all arrays (Fig. 9g,i,k). Deep events (450 m depth) within the array are also well resolved at very high BO, with respective vertical resolutions of 8 m and 6 m for the 2023 and 2024 arrays (Fig. 9n,p,r), despite the trade-off between source depth and phase velocity (Fig. S8), and a horizontal resolution of 2 m for all arrays (Fig. 9t,v,x). Deep events with low BO are significantly less well resolved than surface events. Their vertical resolution decreases to 52 m and 36 m in 2023 and 2024, respectively (Fig. 9m,o,q), and their horizontal resolution decreases to 18 m and 10 m in 2023 and 2024, respectively (Fig. 9s,u,w).

Outside the array, both vertical and horizontal resolutions are poorer than within the array and progressively degrade with increasing distance from it. This loss of resolution is particularly pronounced for low-BO events. Nevertheless, despite the overall degradation outside the array, the horizontal locations of events in the south-western corner of the 2024 array, where no nodes were deployed, remain well resolved even for low-BO events, with horizontal resolutions of 10 m for surface events (Fig. 9i,k) and 15 m for deep events (Fig. 9u,w).

5.3.4 Seasonally varying Bartlett output values: a physical or instrumental origin?

Distinct source types can be recovered by scanning seismic sources across different BO values (Nanni et al., 2022). Based on these results, the decrease in the proportion of HBO surface events that align along crevasses, observed in 2024 compared to spring 2023, can indicate a decrease in surface crevassing activity. To assess whether this shift reflects changes in source processes or instead results from seasonal or instrumental effects, we evaluate how variations in array geometry, sensor tilt, and background noise can influence the BO estimate without changing the underlying event population.

The 2024 array geometry differed from the 2023 configuration, affecting the array response and potentially the convergence of the MFP optimization. A grid-search around each optimized source location shows that optimization-induced mislocations (optimization error) greater than 25 m remain limited to 16% of observed spring 2023 events and only 4% of observed summer 2024 events (Fig. 10a–b). Thus, geometry changes alone cannot explain the systematically lower BO in 2024. Sensor tilt, however, is a more likely contributor. In spring 2023, due to the absence of melt, no sensors were tilted, whereas in 2024 several geophones were moderately tilted, especially during the summer.

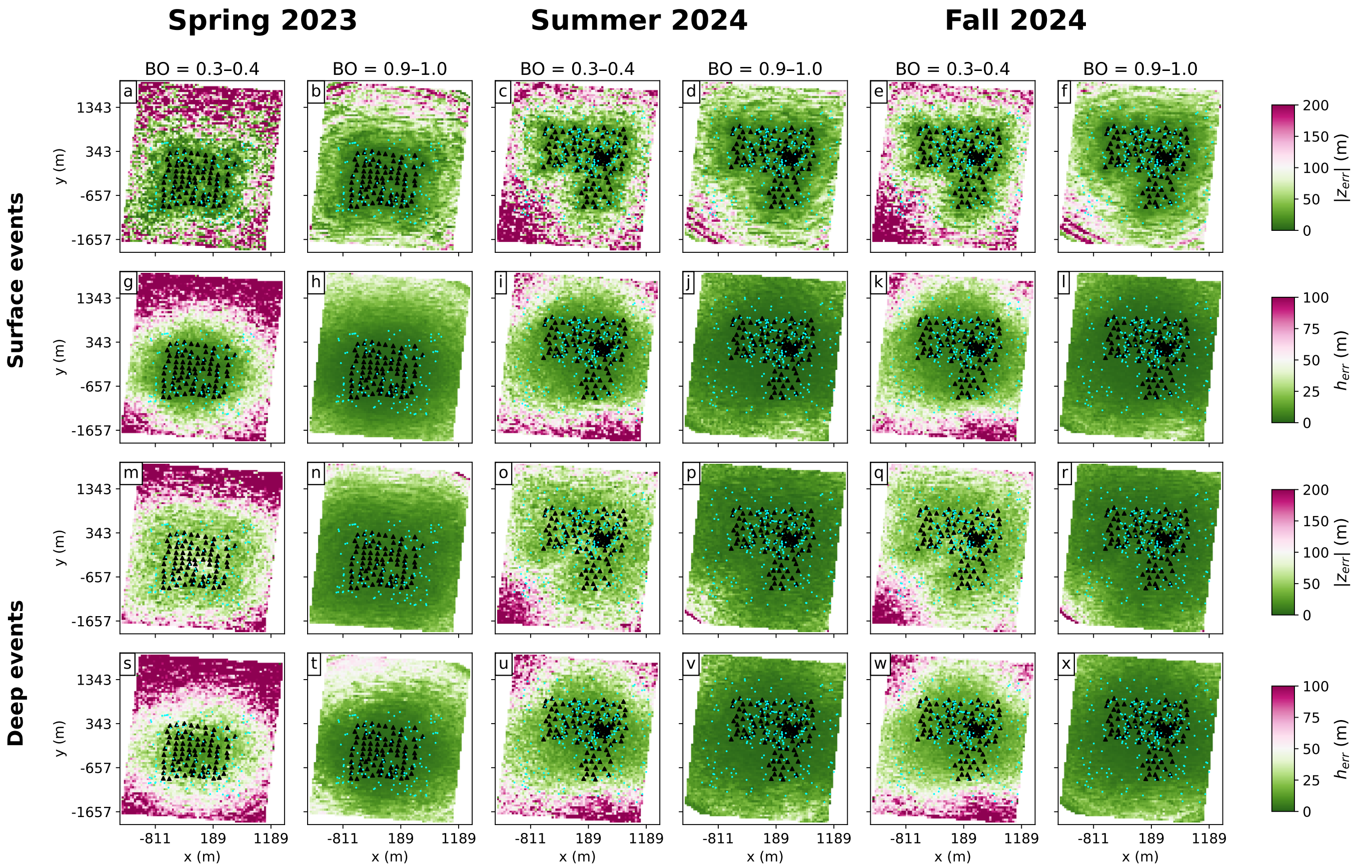

Figure 9 Synthetic resolution tests for a–l) surface events and m–x) deep events (450 m depth) using the spring 2023 (82 nodes; first two columns), summer 2024 (117 nodes; middle two columns), and fall 2024 (115 nodes; last two columns) array geometries. The colormap represents the average error on the vertical direction $|z_{err}|$ and horizontal direction h_{err}. Results in the first, third and fifth columns are obtained from events with BO from 0.3 to 0.4, and those in the second, fourth and sixth columns are obtained from events with BO from 0.9 to 1.0. The cyan dots show the location of starting points used for the optimization. The black triangles show the node locations.

Synthetic tests (details in Subsection S4.2 of the Supplementary Material) show a clear negative correlation between tilt and optimum BO (Fig. 10c), where a mean tilt of 15° is associated with a decrease in optimum BO of ∼0.045. Applying this correction increases the proportion of summer 2024 HBO events to 11.7%, closer to that of spring 2023 statistics.

We measured the noise power between 4–6 Hz in a 1-s time window before each event (Fig. 10d). The background noise level measured in summer 2024 is substantially higher than during other periods, consistent with enhanced surface melt. To quantify the impact of this elevated noise level on maximum BO, we performed synthetic tests (details in Subsection S4.3 of the Supplementary Material). Synthetic events spanning a range of BO values were first generated using the noise level from spring 2023. The SNR of these events was then updated to match the varying noise level across seasons, and MFP optimization was repeated to evaluate BO with the new noise level. These tests show that increased noise reduces BO in a nonlinear manner, with the largest reductions occurring for events that originally exhibit high BO values (Fig. 10e). We use the resulting empirical relationship to estimate the BO values that summer 2024 events would have achieved under the spring 2023 noise level, thereby placing all deployment periods on a common noise baseline. After applying this correction, the proportion of HBO events in summer 2024 increases to ∼14%, matching the proportion observed during spring 2023 (Fig. 10f).

Overall, both sensor tilt and increased background noise contribute significantly to the reduced HBO proportion in summer 2024, with hydrological noise appearing to be the dominant factor. Thus, no evident change in the source types can be inferred from the observed changes in BO values between the different seasons.

6 Discussion

6.1 Using seismic signals from the node array for glacier sources and structure analysis

6.1.1 Glacier sources

Our observations indicate that water flow is a primary source of the ambient seismic noise recorded by the node array. Seismic power is low under no or low melt conditions in early and late summer and is much higher during peak melt in summer (Fig. 5). Seismic power in summer is also particularly strong at low frequencies, as expected if turbulence in the water flow generates tremors (Gimbert et al., 2014, 2016), as ob-

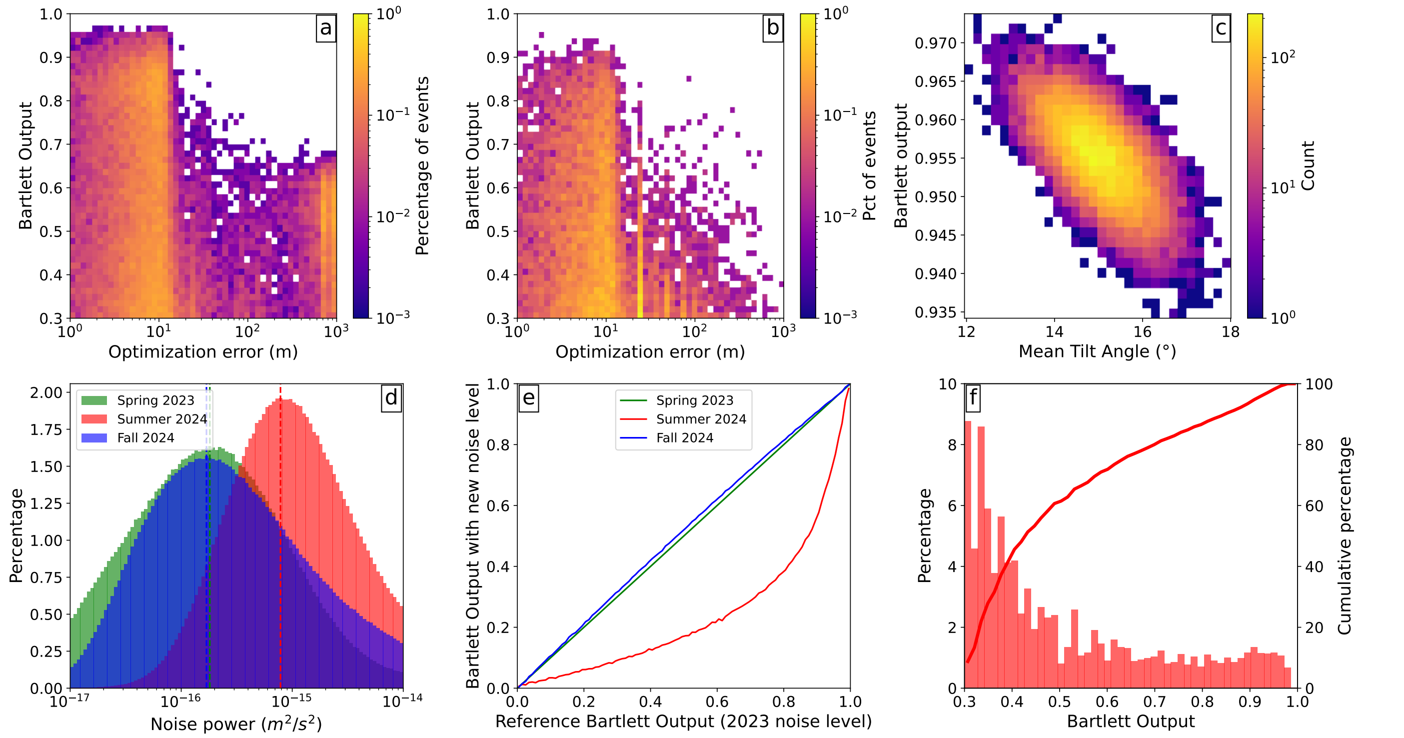

Figure 10 a–b) 2-D histogram of optimization error against Bartlett output, for events observed in a) spring 2023 and b) summer 2024. c) 2-D histogram of maximum Bartlett output against mean sensor tilt angle derived from synthetic tests. d) Histogram of measured noise power for spring 2023 (green), summer 2024 (red), fall 2024 (blue). The vertical dashed lines show the median noise power used in e). e) Bartlett output from synthetic tests using the noise level of each season versus the reference Bartlett output obtained under the spring 2023 noise level. f) Histogram of 2024 Bartlett output corrected for the increase in noise power in summer 2024 with respect to spring 2023. The red curve shows the cumulative percentage of events.

served on other glaciers (Lindner et al., 2020; Nanni et al., 2019; Clyne et al., 2023). The subglacial discharge of Isunnguata Sermia is one of the largest in Greenland (Mankoff et al., 2020), whereas the surface melt in the studied region is fragmented into small catchments, leading to limited surface discharge. Thus, it is likely that subglacial water flow noise dominates over supraglacial water flow noise since seismic power increases with discharge and hydraulic pressure gradient (Gimbert et al., 2014, 2016), which are expected to be larger for subglacial flow. This suggests that the collected dataset can support studies of subglacial hydrology.

Systematic Matched Field Processing (MFP) analysis of Bartlett outputs has been shown to successfully identify englacial and subglacial hydrology under various drainage conditions, from englacial to subglacial cavities and channels (Nanni et al., 2021). However, our results indicate that the quantitative values of the Bartlett output are influenced not only by source characteristics but also by additional factors such as ambient seismic noise, tilt, and array geometry. Noise correlation functions, in combination with principal component analysis, can also be used to locate the largest contributing noise sources and their variations over time (Journeau et al., 2022). An interesting result that supports this approach is that noise correlation functions exhibit high energy near zero lag times in summer (Fig. 6c), when surface melt is large, highlighting an increase in the contribution of sources located inside or below the seismic array.

Seismic sources other than subglacial turbulent water flow operate at the investigated site. Diurnal variability in seismic power from late April to early May 2023 occurs without significant surface melt (Fig. 5c), making it unlikely to be caused by turbulent water flow. We suggest that these sources correspond to englacial fracturing, either driven by temperature changes (Podolskiy et al., 2018) or by hydrodynamic processes (Helmstetter et al., 2015). The most prominent sources obtained at high Bartlett values from MFP exhibit a spatial pattern that follows the surface crevasses distribution (Fig. 8a), similar to previous observations with a dense array on the Argentière alpine glacier (Gimbert et al., 2021; Nanni et al., 2022). This pattern, however, varies across seasons (Fig. 8), which suggests that different types of crevasse activations operate in the different seasons. We show from synthetic analysis (Fig. 9) that super-resolution capabilities (Harris and Kvaerna, 2010) are reached, with errors in source locations ranging from 1 to 18 m horizontally and 6 to 52 m vertically, depending on the Bartlett output and event location. This is promising regarding our ability to discriminate between surface and deep events in order to study crevassing and surface to bed water pathways at high resolution. An interesting insight is our observation that sources attributed to crevassing with MFP are deeper in summer and fall compared to spring (Fig.

8d,f,h), consistent with crevasses extending deeper due to surface melt forcing (van der Veen, 1998).

Of particular interest is the striking agreement between seismic power in the 4–6 Hz band and glacier surface velocities (Fig. 5b), which suggests that ice dynamics are driven by subglacial hydrological processes. The reasons why such a good correlation is obtained here, compared to other glaciers (Umlauft et al., 2023; Bartholomaus et al., 2015; Nanni et al., 2019), remain to be investigated. MFP combined with supervised or unsupervised machine learning (Seydoux et al., 2020) could help decipher the different source mechanisms, allowing for a more targeted analysis of sources primarily associated with changes in ice dynamics.

6.1.2 Glacier structure

We observe differences in the Rayleigh wave phase velocity dispersion curves across the three deployment periods (Fig. 7d–f), particularly between 2023 and 2024. Because the arrays did not cover the same spatial extent in these two years, these differences may partly reflect spatial heterogeneity in seismic velocities associated with variations in ice thickness and/or the presence of englacial and subglacial structures. However, the observed correlation between surface velocity and seismic noise power also suggests that temporal variations in glacier properties may occur. These changes are likely influenced by a combination of surface, englacial, and subglacial features present within the 2.5 km^2 study area, as evidenced by the pronounced spatial variability in surface crevassing. Some of these possible features, such as weakly connected cavities and subglacial lakes, play a key role in bed lubrication properties. They are not necessarily expected to generate seismicity, but they may be resolved through seismic tomography.

The ambient noise correlation functions exhibit clear, stable, and symmetric P and surface wave arrivals, indicating that the ambient noise field is sufficiently diffuse for structural imaging methods, such as surface wave tomography (Shapiro et al., 2005; Nishida et al., 2024) and body wave tomography (Nakata et al., 2015), to be applied seasonally. Rayleigh wave traveltime tomography has already been successfully implemented on the Argentière Glacier (Gimbert et al., 2021). However, glacier settings can exhibit strong seismic azimuthal anisotropy on the order of several percent (Sergeant et al., 2020), which calls for more robust methods such as eikonal tomography that jointly inverts for azimuthal anisotropy (Kästle et al., 2021) or focal spot imaging (Giammarinaro et al., 2022; Hillers et al., 2016; Tsarsitalidou et al., 2024). Surface waves generated by crevassing events also offer unprecedented opportunities for tomography. In particular, Seismic Michelson Interferometry applied to the seismic array, as well as to the source field from turning sources to receivers using the reciprocity principle (Chmiel et al., 2018, 2020; Nanni et al., 2024), can yield constraints at a scale larger than the array and at higher spatial resolutions than those limited by sensor spacing.

Surface wave tomography, however, suffers from limited vertical resolution because the depth sensitivity kernels of surface waves are broad. Moreover, the unconstrained depth of the ice-bed interface would make inferred models from dispersion curves highly nonunique, which is also a major limitation (Lebedev et al., 2013; Nishida et al., 2024). This ambiguity can be reduced by jointly inverting surface wave velocities and Rayleigh wave ellipticity measurements (Hallo et al., 2021). However, surface waves must be of sufficiently low frequency to sample the deep interface, which also limits the horizontal resolution. Other studies have explored the use of P waves to constrain the ice–bed interface. Autocorrelations of teleseismic P wave coda have successfully imaged the ice-rock interface in Antarctica (Phạm and Tkalčić, 2017, 2018), but the low frequencies involved also result in limited resolution, which is insufficient for detailed mapping of bed topography. In contrast, our event catalog includes clear high-frequency P wave arrivals, which can be exploited to study the interface with higher resolution. Surface events generating P waves are expected to allow common reflection analysis analogous to active seismic methods (Booth et al., 2012). Additionally, amplitude versus offset (AVO) analysis (Ostrander, 1984) applied to reflected P waves can provide valuable constraints on the properties of the ice-bed interface and the presence of water. Temporal changes in seismic wave propagation and the underlying structural properties can also be investigated through ambient noise seismic interferometry, applied to ballistic body waves (Brenguier et al., 2020; Sheng et al., 2022), surface waves (Mordret et al., 2020), and coda waves (Mordret et al., 2016; Paris et al., 2025; Zhan, 2019) extracted from noise correlation functions, as well as through icequake coda interferometry (Hillers and Campillo, 2018). By combining these measurements with a velocity model derived from tomography, one can compute sensitivity kernels and thereby constrain the three-dimensional location of seismic velocity variations (Sager et al., 2021).

6.2 On the exploitation of DAS to complement nodes arrays

The dense spatial sampling provided by Distributed Acoustic Sensing (DAS) supports the observation of seismic events and the associated wave propagation at very high frequencies. In contrast, traditional seismic node arrays are fast to deploy and can cover large areas, but their wider station spacing often limits their ability to resolve the wavefield at high frequency. DAS records can also capture slow aseismic deformation (Ouellet et al., 2024), which seismic nodes cannot. Although seismic nodes record vertical and horizontal ground motion, they can experience significant tilt due to surface melt, which particularly affects the data quality in the horizontal components (Fig. 2). DAS, on the contrary, measures strain along the cable axis, providing observations of horizontal ground deformation that are inherently insensitive to sensor tilt when the cable is deployed at the surface. A direct comparison of an icequake recorded by a co-located seismic node and DAS channel (Fig. 7c) demonstrates that, despite uncertain cable-ice coupling due to surface roughness and melt conditions (Fig. 7b), DAS recordings can closely resemble those obtained from conventional seismic sensors, albeit with higher noise level. These characteristics highlight the complementary nature of seismic nodes and DAS measurements and provide strong motivation for their joint deployment in highly dynamic environments such as glaciers.

Both datasets can be combined to perform a joint array analysis of events. However, jointly using DAS and node data for array processing applications requires that they be synchronized in time, which still needs to be established more systematically in our experiments, in addition to being converted to comparable physical quantities using spatial integration and deconvolution. Therefore, unless a rigorous check is performed to ensure time synchronization, the DAS data should be viewed as a complementary tool that offers unique insights into specific aspects of the seismic wavefield that are challenging to capture with the seismic node arrays, such as source migration and rupture length.

6.3 Further improving data quality in future experiments

Across 2023 and 2024, seismic nodes have been affected by two main issues: GNSS signal losses leading to time desynchronization, and sensor tilt. Overall, we observed time desynchronization for 2%, 5%, and 0% of the spring 2023, summer 2024, and fall 2024 datasets, respectively. While GNSS dropouts cannot be fully prevented, they can be straightforward to correct using ambient noise correlation functions. However, these corrections have been made in the 10–20 Hz frequency range and thus may lack precision at higher frequencies, which are important to study basal stick slip, for example (Gimbert et al., 2021; Nap et al., 2025). Sensor tilt, however, remains a primary source of data degradation, and although periods of excessive tilt can be identified through PSD analysis, even moderate tilt (<30°) can significantly distort the signal, as shown by the impact on the MFP Bartlett output. Therefore, a critical improvement is to better control and reduce sensor tilt.

For the 2024 field campaigns, we used Geospace GSB-3 recorders with Geospace GS-ONE LF 5 Hz 3C geophones. These versatile instruments are available from community equipment pools (Hillers et al., 2025), which provide access to the large number of units needed to deploy dense seismic arrays at limited costs. These units can also be connected to external batteries, which extend their autonomy by several months. The main drawback of these sensors compared to the Fairfield units is their geometry. Fairfield sensors are all-in-one cylindrical units, whereas Geospace nodes comprise two to three separate components connected by cables. The shape of the Geospace geophone, combined with the position of the cable connected to the GSB-3, creates additional clearance within the drill hole, leaving the sensor vulnerable to tilt. This issue could be mitigated by placing each sensor inside a casing that fits tightly within the hole. Additionally, deeper holes are expected to help mitigate sensor tilt by allowing quicker refreezing around the sensor, preventing sunlight induced preferential melt at the bottom of the hole, and keeping the sensors buried longer. Such a deployment strategy is possible using an extension cable between the sensor and the logger to ensure the GSB-3 remains near the surface for proper GNSS signal reception. It also requires custom deployment tools to ensure the correct orientation of the sensors toward geographic north.

The main limitation of the DAS dataset is the uncertain coupling with the ice, largely due to surface irregularities and surface streams. The DAS dataset can, therefore, be improved by deploying the optical fiber further upglacier, where there is less surface relief, or in spring when the surface is covered in snow and is free from surface streams. A snow-covered surface is more even, which leads to a better coupled fiber. The fiber can also be deployed in boreholes, where coupling is naturally ensured as the water refreezes around the cable (Booth et al., 2020). This configuration also enables the recording of vertical ground motion, which is currently achieved only by seismic nodes and long-term seismic stations. The SNR of the DAS recordings can also be improved by increasing the number of points per gauge length. Here we used 2 points per gauge length, but using more may help better capture the wavefield at high frequency. The DAS data were only acquired during field campaigns because the interrogator required additional power from a generator. Longer-term DAS acquisitions require the installation of a solar-powered system capable of supplying sufficient energy for continuous and maintenance-free operation.

7 Conclusion

We present a dense, multi-season seismic experiment on the ablation zone of Isunnguata Sermia that is designed to resolve hydrological and dynamic processes at spatial and temporal scales previously inaccessible in Greenland. Each campaign involved continuous one-month data acquisition by an array of 82–117 seismic nodes. In 2024, this was complemented by Distributed Acoustic Sensing (DAS) measurements along two ∼1 km profiles. Rigorous quality control of seismic node records ensured data applicability for array-based analyses despite frequent geophone tilt and GNSS time desynchronization. The DAS records contain signals of seismic events with high spatial resolution, although the data are noisier and also experience episodes of GNSS time desynchronization.

Initial analyses demonstrate that seismic power is dominated by meltwater flow, with strong low-frequency power during peak summer melt, indicating a primarily subglacial origin. This highlights the potential of passive seismic signals as indicators of subglacial hydrological forcing. Seismic power in the 4–6 Hz band closely follows glacier surface velocity, suggesting that ice dynamics are driven by subglacial hydrological processes. Matched Field Processing detects and localizes over a hundred thousand seismic events with meter-scale resolution that reveal characteristic spatial patterns that evolve across seasons. Specifically, surface fracturing occurs in early spring, while deeper events in summer and fall are consistent with melt-driven fracture growth. Ambient noise correlation functions show clear high signal-to-noise ratio Rayleigh, Love, and P wave arrivals. The dispersion curve of Rayleigh waves shows clear variations across datasets that reveal a strong temporal and spatial variability in ice seismic velocities, and that likely reflect heterogeneous surface, englacial, and subglacial structures.

Together, these results confirm the feasibility and value of dense seismic deployments in the ablation zones of rapidly evolving glaciers. These datasets provide an unprecedented perspective for studying the interactions between meltwater input, subglacial drainage evolution, and ice dynamics. Future work will exploit these collected signals to develop high-resolution models of glacier structure, characterize hydrological pathways across melt seasons, and improve our understanding of the processes driving the dynamics of the Greenland Ice Sheet.

Acknowledgements

This study was funded by the European Research Council (ERC) under grant number 101126009 (REASSESS), the UK's Natural Environment Research Council (NERC) under grant number NE/X000257/1 (SLIDE) and by the Research Council of Finland (Flagship of Advanced Mathematics for Sensing, Imaging, and Modelling grant 359182). MRPJ, JDH, and LC were supported by a UKRI Future Leaders Fellowship (MR/V022237/1). TRC was supported by a Leverhulme Early Career Fellowship (ECF-2022-589). Part of the instruments used for data collection are those of Epos-France's Sismob mobile seismological park (sismob.epos-france.fr) (INSU-CNRS). All the computations presented in this paper were performed using the GRICAD infrastructure (https://gricad.univ-grenoble-alpes.fr), which is supported by Grenoble research communities, and with the CiGri tool (https://github.com/oar-team/cigri) developed by Gricad, Grid5000 (https://www.grid5000.fr) and LIG (https://www.liglab.fr/). We acknowledge the support of Kangerlussuaq International Science Support and Chris Sorensen in providing logistical support. We thank Olivier Coutant for his help with the DAS parametrization; Florent Brenguier, Coralie Aubert, and Marcella Pineda for sharing their experience with Geospace instruments; Luc Piard and Romain Duphil for designing the geophone deployment stick; and Aurélien Mordret for providing the 2024 node deployment coordinates following the specter geometry. The authors thank two anonymous reviewers for their comments and suggestions which improved the quality and clarity of this manuscript.

Data and resources availability

The seismological data used are provided by the Epos-France datacenter (Péquegnat et al., 2021) and through the European Integrated Data Archive (EIDA, Strollo et al. (2021)). The 2023 (10.15778/RESIF.9F2023) and 2024 (10.7914/a9fc-5r56) array and long-term seismic data will be publicly available under the FDSN network code "9F" by January 2027. The DAS data are currently unavailable for online download due to the absence of a suitable distribution platform; however, they can be provided upon request. The outlet station Radian data will be made publicly available by 2027. The GNSS data are available on request and will be uploaded to the NERC Polar Data Centre by January 2027. The resources to reproduce the results, such as clock correction files, tilt and event catalogs, etc. can be accessed in the following repository: 10.5281/zenodo.17369235.

Competing interests

The authors declare that they have no competing interests.

References

Andrews, L. C., Catania, G. A., Hoffman, M. J., Gulley, J. D., Lüthi, M. P., Ryser, C., Hawley, R. L., and Neumann, T. A. Direct observations of evolving subglacial drainage beneath the Greenland Ice Sheet. *Nature*, 514(7520):80–83, 2014. doi: 10.1038/nature13796.

Baggeroer, A. B., Kuperman, W. A., and Schmidt, H. Matched field processing: Source localization in correlated noise as an optimum parameter estimation problem. *The Journal of the Acoustical Society of America*, 83(2):571–587, 1988. doi: 10.1121/1.396151.

Bartholomaus, T. C., Amundson, J. M., Walter, J. I., O'Neel, S., West, M. E., and Larsen, C. F. Subglacial discharge at tidewater glaciers revealed by seismic tremor. *Geophysical Research Letters*, 42 (15):6391–6398, 2015. doi: 10.1002/2015GL064590.

Booth, A. D., Clark, R. A., Kulessa, B., Murray, T., Carter, J., Doyle, S., and Hubbard, A. Thin-layer effects in glaciological seismic amplitude-versus-angle (AVA) analysis: implications for characterising a subglacial till unit, Russell Glacier, West Greenland. *The Cryosphere*, 6(4):909–922, 2012. doi: 10.5194/tc-6-909-2012.

Booth, A. D., Christoffersen, P., Schoonman, C., Clarke, A., Hubbard, B., Law, R., Doyle, S. H., Chudley, T. R., and Chalari, A. Distributed Acoustic Sensing of Seismic Properties in a Borehole Drilled on a Fast-Flowing Greenlandic Outlet Glacier. *Geophysical Research Letters*, 47(13):e2020GL088148, 2020. doi: 10.1029/2020GL088148.

Brenguier, F., Courbis, R., Mordret, A., Campman, X., Boué, P., Chmiel, M., Takano, T., Lecocq, T., Van der Veen, W., Postif, S., and Hollis, D. Noise-based ballistic wave passive seismic monitoring. Part 1: body waves. *Geophysical Journal International*, 221(1):683–691, 2020. doi: 10.1093/gji/ggz440.

Campillo, M. and Paul, A. Long-Range Correlations in the Diffuse Seismic Coda. *Science*, 299(5606):547–549, 2003. doi: 10.1126/science.1078551.

Chandler, D. M., Wadham, J. L., Lis, G. P., Cowton, T., Sole, A., Bartholomew, I., Telling, J., Nienow, P., Bagshaw, E. B., Mair, D., Vinen, S., and Hubbard, A. Evolution of the subglacial drainage system beneath the Greenland Ice Sheet revealed by tracers. *Nature Geoscience*, 6(3):195–198, 2013. doi: 10.1038/ngeo1737.

Chen, G. *GPS Kinematic Positioning for the Airborne Laser Altimetry at Long Valley, California*. Phd thesis, Massachusetts Institute of Technology, Cambridge, MA, 1998.

Chmiel, M., Roux, P., Herrmann, P., Rondeleux, B., and Wathelet, M. Data-based diffraction kernels for surface waves from convolution and correlation processes through active seismic interferometry. *Geophysical Journal International*, 214(2):1468–1480, 2018. doi: 10.1093/gji/ggy211.

Chmiel, M., Roux, P., and Bardainne, T. High-sensitivity microseismic monitoring: Automatic detection and localization of subsurface noise sources using matched-field processing and dense patch arrays. *GEOPHYSICS*, 84(6):KS211–KS223, 2019. doi: 10.1190/geo2018-0537.1.

Chmiel, M., Roux, P., Wathelet, M., and Bardainne, T. Phase-velocity inversion from data-based diffraction kernels: seismic Michelson interferometer. *Geophysical Journal International*, 224(2):1287–1300, 2020. doi: 10.1093/gji/ggaa512.

Chu, W., Schroeder, D. M., Seroussi, H., Creyts, T. T., Palmer, S. J., and Bell, R. E. Extensive winter subglacial water storage beneath the Greenland Ice Sheet. *Geophysical Research Letters*, 43(24): 12,484–12,492, 2016. doi: 10.1002/2016GL071538.

Clyne, E., Alley, R. B., Vore, M., Gräff, D., Anandakrishnan, S., Walter, F., and Sergeant, A. Glacial hydraulic tremor on Rhonegletscher, Switzerland. *Journal of Glaciology*, 69(274):370–380, 2023. doi: 10.1017/jog.2022.69.

Dow, J. M., Neilan, R. E., and Rizos, C. The International GNSS Service in a changing landscape of Global Navigation Satellite Systems. *Journal of Geodesy*, 83(3):191–198, 2009. doi: 10.1007/s00190-008-0300-3.

Fausto, R. S., Van As, D., Mankoff, K. D., Vandecrux, B., Citterio, M., Ahlstrøm, A. P., Andersen, S. B., Colgan, W., Karlsson, N. B., Kjeldsen, K. K., Korsgaard, N. J., Larsen, S. H., Nielsen, S., Pedersen, A. Ø., Shields, C. L., Solgaard, A. M., and Box, J. E. Programme for Monitoring of the Greenland Ice Sheet (PROMICE) automatic weather station data. *Earth System Science Data*, 13 (8):3819–3845, 2021. doi: 10.5194/essd-13-3819-2021.

Fichtner, A., Hofstede, C., Kennett, B. L. N., Svensson, A., Westhoff, J., Walter, F., Ampuero, J.-P., Cook, E., Zigone, D., Jansen, D., and Eisen, O. Hidden cascades of seismic ice stream deformation. *Science*, 387(6736):858–864, 2025. doi: 10.1126/science.adp8094.

Flowers, G. E. Modelling water flow under glaciers and ice sheets. *Proceedings of the Royal Society A: Mathematical, Physical and Engineering Sciences*, 471(2176):20140907, 2015. doi: 10.1098/rspa.2014.0907.

Fudge, T., Humphrey, N. F., Harper, J. T., and Tad Pfeffer, W. Diurnal fluctuations in borehole water levels: configuration of the drainage system beneath Bench Glacier, Alaska, USA. *Journal of Glaciology*, 54(185):297–306, 2008. doi: 10.3189/002214308784886072.

Gagliardini, O., Cohen, D., Råback, P., and Zwinger, T. Finite-element modeling of subglacial cavities and related friction law. *Journal of Geophysical Research: Earth Surface*, 112(F2), 2007. doi: 10.1029/2006JF000576.

Giammarinaro, B., Tsarsitalidou, C., Hillers, G., de Rosny, J., Seydoux, L., Catheline, S., Campillo, M., and Roux, P. Seismic surface wave focal spot imaging: numerical resolution experiments. *Geophysical Journal International*, 232(1):201–222, 2022. doi: 10.1093/gji/ggac247.

Gimbert, F., Tsai, V. C., and Lamb, M. P. A physical model for seismic noise generation by turbulent flow in rivers. *Journal of Geophysical Research: Earth Surface*, 119(10):2209–2238, 2014. doi: 10.1002/2014JF003201.

Gimbert, F., Tsai, V. C., Amundson, J. M., Bartholomaus, T. C., and Walter, J. I. Subseasonal changes observed in subglacial channel pressure, size, and sediment transport. *Geophysical Research Letters*, 43(8):3786–3794, 2016. doi: 10.1002/2016GL068337.

Gimbert, F., Nanni, U., Roux, P., Helmstetter, A., Garambois, S., Lecointre, A., Walpersdorf, A., Jourdain, B., Langlais, M., Laarman, O., Lindner, F., Sergeant, A., Vincent, C., and Walter, F. A Multi-Physics Experiment with a Temporary Dense Seismic Array on the Argentière Glacier, French Alps: The RESOLVE Project. *Seismological Research Letters*, 92(2A):1185–1201, 2021. doi: 10.1785/0220200280.

Hallo, M., Imperatori, W., Panzera, F., and Fäh, D. Joint multizonal transdimensional Bayesian inversion of surface wave dispersion and ellipticity curves for local near-surface imaging. *Geophysical Journal International*, 226(1):627–659, 2021. doi: 10.1093/gji/ggab116.

Harper, J., Hubbard, A., Ruskeeniemi, T., Claesson Liljedahl, L., Lehtinen, A., Booth, A., Brinkerhoff, D., Drake, H., Dow, C., Doyle, S., Engström, J., Fitzpatrick, A., Frape, S., Henkemans, E., Humphrey, N., Johnson, J., Jones, G., Joughin, I., Klint, K., Kukkonen, I., Kulessa, B., Landowski, C., Lindbäck, K., Makahnouk, M., Meierbachtol, T., Pere, T., Pedersen, K., Pettersson, R., Pimentel, S., Quincey, D., Tullborg, E.-L., and van As, D. *The Greenland Analogue Project. Yearly Report 2010*. The Greenland Analogue Project. Yearly Report. Svensk Kärnbränslehantering AB, 2011.

Harper, J. T., Humphrey, N. F., Meierbachtol, T. W., Graly, J. A., and Fischer, U. H. Borehole measurements indicate hard bed conditions, Kangerlussuaq sector, western Greenland Ice Sheet. *Journal of Geophysical Research: Earth Surface*, 122(9):1605–1618, 2017. doi: 10.1002/2017JF004201.

Harrington, J. A., Humphrey, N. F., and Harper, J. T. Temperature distribution and thermal anomalies along a flowline of the Greenland ice sheet. *Annals of Glaciology*, 56(70):98–104, 2015. doi: 10.3189/2015AoG70A945.

Harris, D. B. and Kvaerna, T. Superresolution with seismic arrays using empirical matched field processing. *Geophysical Journal International*, 182(3):1455–1477, 2010. doi: 10.1111/j.1365-246x.2010.04684.x.

Helmstetter, A., Moreau, L., Nicolas, B., Comon, P., and Gay, M. Intermediate-depth icequakes and harmonic tremor in an Alpine glacier (Glacier d'Argentière, France): Evidence for hydraulic fracturing? *Journal of Geophysical Research: Earth Surface*, 120(3):402–416, 2015. doi: 10.1002/2014JF003289.

Hillers, G. and Campillo, M. Fault Zone Imaging from Correlations of Aftershock Waveforms. *Pure and Applied Geophysics*, 175(8): 2643–2667, 2018. doi: 10.1007/s00024-018-1836-7.

Hillers, G., Roux, P., Campillo, M., and Ben-Zion, Y. Focal spot imaging based on zero lag cross-correlation amplitude fields: Application to dense array data at the San Jacinto fault zone. *Journal of Geophysical Research: Solid Earth*, 121(11):8048–8067, 2016. doi: 10.1002/2016JB013014.

Hillers, G., Koivisto, E., Haapanala, P., Kukkonen, I., Courbis, R., Ding, Y., Fordell, T., Heinonen, S., Junno, N., Juntunen, A., Komminaho, K., Kozlovskaya, E., Leveinen, J., Moisio, K., Näränen, J., Oksanen, T., Skyttä, P., Tanskanen, E., and Tiira, T. FINNSIP - The mobile Finnish Seismic Instrument Pool. *Seismica*, 4(1), 2025. doi: 10.26443/seismica.v4i1.1379.

Horgan, H. J., Anderson, B., Alley, R. B., Chamberlain, C. J., Dykes, R., Kehrl, L. M., and Townend, J. Glacier velocity variability due to rain-induced sliding and cavity formation. *Earth and Planetary Science Letters*, 432:273–282, 2015. doi: 10.1016/j.epsl.2015.10.016.

Jezek, K., Wu, X., Paden, J., and Leuschen, C. Radar mapping of Isunnguata Sermia, Greenland. *Journal of Glaciology*, 59(218): 1135–1146, 2013. doi: 10.3189/2013JoG12J248.

Jones, C., Ryan, J., Holt, T., and Hubbard, A. Structural glaciology of Isunguata Sermia, West Greenland. *Journal of Maps*, 14(2): 517–527, Nov. 2018. doi: 10.1080/17445647.2018.1507952.

Jones, G., Kulessa, B., Doyle, S., Dow, C., and Hubbard, A. An automated approach to the location of icequakes using seismic waveform amplitudes. *Annals of Glaciology*, 54(64):1–9, 2013. doi: 10.3189/2013AoG64A074.

Journeau, C., Shapiro, N. M., Seydoux, L., Soubestre, J., Koulakov, I. Y., Jakovlev, A. V., Abkadyrov, I., Gordeev, E. I., Chebrov, D. V., Droznin, D. V., Sens-Schönfelder, C., Luehr, B. G., Tong, F., Farge, G., and Jaupart, C. Seismic tremor reveals active trans-crustal magmatic system beneath Kamchatka volcanoes. *Science Advances*, 8(5):eabj1571, 2022. doi: 10.1126/sciadv.abj1571.

King, M. Rigorous GPS data-processing strategies for glaciological applications. *Journal of Glaciology*, 50(171):601–607, 2004. doi: 10.3189/172756504781829747.

Kästle, E. D., Molinari, I., Boschi, L., Kissling, E., and and the AlpArray Working Group. Azimuthal anisotropy from eikonal tomography: example from ambient-noise measurements in the AlpArray network. *Geophysical Journal International*, 229(1): 151–170, 2021. doi: 10.1093/gji/ggab453.

Lebedev, S., Adam, J. M.-C., and Meier, T. Mapping the Moho with seismic surface waves: A review, resolution analysis, and recommended inversion strategies. *Tectonophysics*, 609:377–394, 2013. doi: 10.1016/j.tecto.2012.12.030.

Lindbäck, K., Pettersson, R., Doyle, S. H., Helanow, C., Jansson, P., Kristensen, S. S., Stenseng, L., Forsberg, R., and Hubbard, A. L. High-resolution ice thickness and bed topography of a land-terminating section of the Greenland Ice Sheet. *Earth System Science Data*, 6(2):331–338, 2014. doi: 10.5194/essd-6-331-2014.

Lindner, F., Walter, F., Laske, G., and Gimbert, F. Glaciohydraulic seismic tremors on an Alpine glacier. *The Cryosphere*, 14(1): 287–308, Jan. 2020. doi: 10.5194/tc-14-287-2020.

Livingstone, S. J., Sole, A. J., Storrar, R. D., Harrison, D., Ross, N., and Bowling, J. Brief communication: Subglacial lake drainage beneath Isunguata Sermia, West Greenland: geomorphic and ice dynamic effects. *The Cryosphere*, 13(10):2789–2796, 2019. doi: 10.5194/tc-13-2789-2019.

Lliboutry, L. General Theory of Subglacial Cavitation and Sliding of Temperate Glaciers. *Journal of Glaciology*, 7(49):21–58, 1968. doi: 10.3189/S0022143000020396.

Maier, N., Gimbert, F., and Gillet-Chaulet, F. Threshold response to melt drives large-scale bed weakening in Greenland. *Nature*, 607(7920):714–720, 2022. doi: 10.1038/s41586-022-04927-3.

Mankoff, K. D., Noël, B., Fettweis, X., Ahlstrøm, A. P., Colgan, W., Kondo, K., Langley, K., Sugiyama, S., van As, D., and Fausto, R. S. Greenland liquid water discharge from 1958 through 2019. *Earth System Science Data*, 12(4):2811–2841, 2020. doi: 10.5194/essd-12-2811-2020.

Manos, J.-M., Gräff, D., Martin, E. R., Paitz, P., Walter, F., Fichtner, A., and Lipovsky, B. P. DAS to discharge: using distributed acoustic sensing (DAS) to infer glacier runoff. *Journal of Glaciology*, 70: e67, 2024. doi: 10.1017/jog.2024.46.

Meierbachtol, T., Harper, J., and Humphrey, N. Basal Drainage System Response to Increasing Surface Melt on the Greenland Ice Sheet. *Science*, 341(6147):777–779, 2013. doi: 10.1126/science.1235905.

Mordret, A. and Grushin, A. G. Beating the aliasing limit with aperiodic monotile arrays. *Physical Review Applied*, 23(3):034021, 2025. doi: 10.1103/PhysRevApplied.23.034021.

Mordret, A., Mikesell, T. D., Harig, C., Lipovsky, B. P., and Prieto, G. A. Monitoring southwest Greenland's ice sheet melt with ambient seismic noise. *Science Advances*, 2(5):e1501538, 2016. doi: 10.1126/sciadv.1501538.

Mordret, A., Courbis, R., Brenguier, F., Chmiel, M., Garambois, S., Mao, S., Boué, P., Campman, X., Lecocq, T., Van der Veen, W., and Hollis, D. Noise-based ballistic wave passive seismic monitoring – Part 2: surface waves. *Geophysical Journal International*, 221(1):692–705, 2020. doi: 10.1093/gji/ggaa016.

Morlighem, M., Williams, C. N., Rignot, E., An, L., Arndt, J. E., Bamber, J. L., Catania, G., Chauché, N., Dowdeswell, J. A., Dorschel, B., Fenty, I., Hogan, K., Howat, I., Hubbard, A., Jakobsson, M., Jordan, T. M., Kjeldsen, K. K., Millan, R., Mayer, L., Mouginot, J., Noël, B. P. Y., O'Cofaigh, C., Palmer, S., Rysgaard, S., Seroussi, H., Siegert, M. J., Slabon, P., Straneo, F., van den Broeke, M. R., Weinrebe, W., Wood, M., and Zinglersen, K. B. BedMachine v3: Complete Bed Topography and Ocean Bathymetry Mapping of Greenland From Multibeam Echo Sounding Combined With Mass Conservation. *Geophysical Research Letters*, 44(21), 2017. doi: 10.1002/2017GL074954.

Mouginot, J., Rignot, E., Bjørk, A. A., van den Broeke, M., Millan, R., Morlighem, M., Noël, B., Scheuchl, B., and Wood, M. Forty-six years of Greenland Ice Sheet mass balance from 1972 to 2018. *Proceedings of the National Academy of Sciences*, 116(19): 9239–9244, 2019. doi: 10.1073/pnas.1904242116.

Muñoz-Sabater, J., Dutra, E., Agustí-Panareda, A., Albergel, C., Arduini, G., Balsamo, G., Boussetta, S., Choulga, M., Harrigan, S., Hersbach, H., Martens, B., Miralles, D. G., Piles, M., Rodríguez-Fernández, N. J., Zsoter, E., Buontempo, C., and Thépaut, J.-N. ERA5-Land: a state-of-the-art global reanalysis dataset for land applications. *Earth System Science Data*, 13(9):4349–4383, 2021. doi: 10.5194/essd-13-4349-2021.

Murray, T. and Clarke, G. K. C. Black-box modeling of the subglacial water system. *Journal of Geophysical Research: Solid Earth*, 100 (B6):10231–10245, 1995. doi: 10.1029/95JB00671.

Nakata, N., Chang, J. P., Lawrence, J. F., and Boué, P. Body wave extraction and tomography at Long Beach, California, with ambient-noise interferometry. *Journal of Geophysical Research: Solid Earth*, 120(2):1159–1173, 2015. doi: 10.1002/2015JB011870.

Nanni, U., Gimbert, F., Vincent, C., Gräff, D., Walter, F., Piard, L., and Moreau, L. Seasonal and Diurnal Dynamics of Subglacial Channels: Observations Beneath an Alpine Glacier. *The Cryosphere Discussions*, pages 1–31, 2019. doi: 10.5194/tc-2019-243.

Nanni, U., Gimbert, F., Roux, P., and Lecointre, A. Observing the subglacial hydrology network and its dynamics with a dense seismic array. *Proceedings of the National Academy of Sciences*, 118(28):e2023757118, 2021. doi: 10.1073/pnas.2023757118.

Nanni, U., Roux, P., Gimbert, F., and Lecointre, A. Dynamic Imaging of Glacier Structures at High-Resolution Using Source Localization With a Dense Seismic Array. *Geophysical Research Letters*, 49(6):e2021GL095996, 2022. doi: 10.1029/2021GL095996.

Nanni, U., Roux, P., and Gimbert, F. Mapping Glacier Structure in Inaccessible Areas From Turning Seismic Sources Into a Dense Seismic Array. *Geophysical Research Letters*, 51(11): e2023GL108058, 2024. doi: 10.1029/2023GL108058.

Nap, A., Hudson, T., Walter, F., Wehrlé, A., Kneib-Walter, A., Rousseau, H., and Lüthi, M. P. Interpreting Ice Anisotropy of Greenland's Fastest Outlet Glacier Using Basal Icequakes. *Geophysical Research Letters*, 52(12):e2025GL116225, 2025. doi: 10.1029/2025GL116225.

Nath, P. C. and Vaughan, D. G. Subsurface crevasse formation in glaciers and ice sheets. *Journal of Geophysical Research: Solid Earth*, 108(B1):ECV 7–1–ECV 7–12, 2003. doi: 10.1029/2001JB000453.

Nelder, J. A. and Mead, R. A Simplex Method for Function Minimization. *The Computer Journal*, 7(4):308–313, 1965. doi: 10.1093/comjnl/7.4.308.

Nishida, K., Takagi, R., and Takeo, A. Ambient noise multimode surface wave tomography. *Progress in Earth and Planetary Science*, 11(1):4, 2024. doi: 10.1186/s40645-023-00605-8.

Ostrander, W. J. Plane-Wave Reflection Coefficients for Gas Sands at Nonnormal Angles of Incidence. *Exploration Geophysics*, 15 (3):193–193, 1984. doi: 10.1071/EG984193a.

Ouellet, S. M., Dettmer, J., Lato, M. J., Cole, S., Hutchinson, D. J., Karrenbach, M., Dashwood, B., Chambers, J. E., and Crickmore, R. Previously hidden landslide processes revealed using distributed acoustic sensing with nanostrain-rate sensitivity. *Nature Communications*, 15(1):6239, Jul 2024. doi: 10.1038/s41467-024-50604-6.

Paris, N., Itoh, Y., Brenguier, F., Wang, Q.-Y., Sheng, Y., Okada, T., Uchida, N., Higueret, Q., Takagi, R., Sakai, S., Hirahara, S., and Kimura, S. Coseismic crustal seismic velocity changes associated with the 2024 MW 7.5 Noto earthquake, Japan. *Earth, Planets and Space*, 77(1):51, 2025. doi: 10.1186/s40623-025-02177-x.

Park, C. B., Miller, R. D., and Xia, J. *Imaging dispersion curves of surface waves on multi-channel record*, pages 1377–1380. Society of Exploration Geophysicists, 2005. doi: 10.1190/1.1820161.

Phạm, T.-S. and Tkalčić, H. On the feasibility and use of teleseismic *P* wave coda autocorrelation for mapping shallow seismic discontinuities. *Journal of Geophysical Research: Solid Earth*, 122 (5):3776–3791, 2017. doi: 10.1002/2017JB013975.

Phạm, T.-S. and Tkalčić, H. Antarctic Ice Properties Revealed From Teleseismic *P* Wave Coda Autocorrelation. *Journal of Geophysical Research: Solid Earth*, 123(9):7896–7912, 2018. doi: 10.1029/2018JB016115.

Podolskiy, E. A., Fujita, K., Sunako, S., Tsushima, A., and Kayastha, R. B. Nocturnal Thermal Fracturing of a Himalayan Debris-Covered Glacier Revealed by Ambient Seismic Noise. *Geophysical Research Letters*, 45(18):9699–9709, 2018. doi: 10.1029/2018GL079653.

Péquegnat, C., Schaeffer, J., Satriano, C., Pedersen, H., Touvier, J., Saurel, J., Calvet, M., Stehly, L., Arnoul, P., Bollard, P., Dewée, O., Engels, F., Grunberg, M., Pardo, C., Wolyniec, D., Arneodo, G., Bouazzouz, R., Geber, O., Aubert, C., Langlais, M., Roussel, S., Brenguier, F., Crawford, W. C., Lemarchand, A., Maufroy, E., Olivier, S., Rivet, D., Vallée, M., Vergne, J., Chèze, J., Debayle, E., Delouis, B., Guéguen, P., Lambotte, S., Mocquet, A., Paul, A., Peix, F., Schindelé, F., Shapiro, N., Stutzmann, E., Volcke, P., and Walpersdorf, A. RÉSIF-SI: A Distributed Information System for French Seismological Data. *Seismological Research Letters*, 92 (3):1832–1853, 04 2021. doi: 10.1785/0220200392.

Rada, C. and Schoof, C. Channelized, distributed, and disconnected: subglacial drainage under a valley glacier in the Yukon. *The Cryosphere*, 12(8):2609–2636, 2018. doi: 10.5194/tc-12-2609-2018.

Rignot, E., Mouginot, J., Scheuchl, B., van den Broeke, M., van Wessem, M. J., and Morlighem, M. Four decades of Antarctic Ice Sheet mass balance from 1979–2017. *Proceedings of the National Academy of Sciences*, 116(4):1095–1103, 2019. doi: 10.1073/pnas.1812883116.

Ringler, A. T., Anthony, R. E., Karplus, M. S., Holland, A. A., and Wilson, D. C. Laboratory Tests of Three Z-Land Fairfield Nodal 5-Hz, Three-Component Sensors. *Seismological Research Letters*, 89 (5):1601–1608, 2018. doi: 10.1785/0220170236.

Roeoesli, C., Helmstetter, A., Walter, F., and Kissling, E. Meltwater influences on deep stick-slip icequakes near the base of the Greenland Ice Sheet. *Journal of Geophysical Research: Earth Surface*, 121(2):223–240, 2016. doi: 10.1002/2015JF003601.

Röösli, C., Walter, F., Husen, S., Andrews, L. C., Lüthi, M. P., Catania, G. A., and Kissling, E. Sustained seismic tremors and icequakes detected in the ablation zone of the Greenland ice sheet. *Journal of Glaciology*, 60(221):563–575, 2014. doi: 10.3189/2014JoG13J210.

Sager, K., Tsai, V. C., Sheng, Y., Brenguier, F., Boué, P., Mordret, A., and Igel, H. Modelling *P* waves in seismic noise correlations: advancing fault monitoring using train traffic sources. *Geophysical Journal International*, 228(3):1556–1567, 2021. doi: 10.1093/gji/ggab389.

Sauter, T., Arndt, A., and Schneider, C. COSIPY v1.3 – an open-source coupled snowpack and ice surface energy and mass balance model. *Geoscientific Model Development*, 13(11): 5645–5662, 2020. doi: 10.5194/gmd-13-5645-2020.

Schoof, C. The Effect of Cavitation on Glacier Sliding. *Proceedings: Mathematical, Physical and Engineering Sciences*, 461(2055): 609–627, 2005. http://www.jstor.org.sid2nomade-2.grenet.fr/stable/30046308.

Schoof, C. Ice-sheet acceleration driven by melt supply variability. *Nature*, 468(7325):803–806, 2010. doi: 10.1038/nature09618.

Sergeant, A., Chmiel, M., Lindner, F., Walter, F., Roux, P., Chaput, J., Gimbert, F., and Mordret, A. On the Green's function emergence from interferometry of seismic wave fields generated in high-melt glaciers: implications for passive imaging and monitoring. *The Cryosphere*, 14(3):1139–1171, 2020. doi: 10.5194/tc-14-1139-2020.

Seydoux, L., Balestriero, R., Poli, P., Hoop, M. d., Campillo, M., and Baraniuk, R. Clustering earthquake signals and background noises in continuous seismic data with unsupervised deep learning. *Nature Communications*, 11(1):3972, 2020. doi: 10.1038/s41467-020-17841-x.

Shapiro, N. M., Campillo, M., Stehly, L., and Ritzwoller, M. H. High-Resolution Surface-Wave Tomography from Ambient Seismic Noise. *Science*, 307(5715):1615–1618, 2005. doi: 10.1126/science.1108339.

Sheng, Y., Mordret, A., Sager, K., Brenguier, F., Boué, P., Rousset, B., Vernon, F., Higueret, Q., and Ben-Zion, Y. Monitoring Seismic Velocity Changes Across the San Jacinto Fault Using Train-Generated Seismic Tremors. *Geophysical Research Letters*, 49 (19):e2022GL098509, 2022. doi: 10.1029/2022GL098509.

Stehly, L., Campillo, M., and Shapiro, N. M. Traveltime measurements from noise correlation: stability and detection of instrumental time-shifts. *Geophysical Journal International*, 171(1): 223–230, 2007. doi: 10.1111/j.1365-246X.2007.03492.x.

Strollo, A., Cambaz, D., Clinton, J., Danecek, P., Evangelidis, C. P., Marmureanu, A., Ottemöller, L., Pedersen, H., Sleeman, R., Stammler, K., Armbruster, D., Bienkowski, J., Boukouras, K., Evans, P. L., Fares, M., Neagoe, C., Heimers, S., Heinloo, A., Hoffmann, M., Kaestli, P., Lauciani, V., Michalek, J., Odon Muhire, E., Ozer, M., Palangeanu, L., Pardo, C., Quinteros, J., Quintiliani, M., Antonio Jara-Salvador, J., Schaeffer, J., Schloemer, A., and Triantafyllis, N. EIDA: The European Integrated Data Archive and Service Infrastructure within ORFEUS. *Seismological Research Letters*, 92(3):1788–1795, 03 2021. doi: 10.1785/0220200413.

Togaibekov, A., Gimbert, F., Gilbert, A., and Walpersdorf, A. Observing and Modeling Short-Term Changes in Basal Friction During Rain-Induced Speed-Ups on an Alpine Glacier. *Geophysical Research Letters*, 51(14):e2023GL107999, 2024. doi: 10.1029/2023GL107999.

Trabattoni, A., Biagioli, F., Strumia, C., van den Ende, M., Scotto di Uccio, F., Festa, G., Rivet, D., Sladen, A., Ampuero, J. P., Metaxian, J.-P., and Stutzmann, E. From strain to displacement: using deformation to enhance distributed acoustic sensing applications. *Geophysical Journal International*, 235(3):2372–2384, 2023. doi: 10.1093/gji/ggad365.

Tsarsitalidou, C., Hillers, G., Giammarinaro, B., Boué, P., Stehly, L., and Campillo, M. Long Period Rayleigh Wave Focal Spot Imaging Applied to USArray Data. *Journal of Geophysical Research: Solid Earth*, 129(5):e2023JB027417, 2024. doi:

10.1029/2023JB027417.

Umlauft, J., Johnson, C. W., Roux, P., Trugman, D. T., Lecointre, A., Walpersdorf, A., Nanni, U., Gimbert, F., Rouet-Leduc, B., Hulbert, C., Lüdtke, S., Marton, S., and Johnson, P. A. Mapping Glacier Basal Sliding Applying Machine Learning. *Journal of Geophysical Research: Earth Surface*, 128(11):e2023JF007280, 2023. doi: 10.1029/2023JF007280.

Van den Broeke, M., Box, J., Fettweis, X., Hanna, E., Noël, B., Tedesco, M., van As, D., Berg, W., and van Kampenhout, L. Greenland Ice Sheet Surface Mass Loss: Recent Developments in Observation and Modeling. *Current Climate Change Reports*, 3, 2017. doi: 10.1007/s40641-017-0084-8.

van der Veen, C. J. Fracture mechanics approach to penetration of surface crevasses on glaciers. *Cold Regions Science and Technology*, 27(1):31–47, 1998. doi: 10.1016/S0165-232X(97)00022-0.

Walter, F., Gräff, D., Lindner, F., Paitz, P., Köpfli, M., Chmiel, M., and Fichtner, A. Distributed acoustic sensing of microseismic sources and wave propagation in glaciated terrain. *Nature Communications*, 11(1):2436, 2020. doi: 10.1038/s41467-020-15824-6.

Zhan, Z. Seismic Noise Interferometry Reveals Transverse Drainage Configuration Beneath the Surging Bering Glacier. *Geophysical Research Letters*, 46(9):4747–4756, 2019. doi: 10.1029/2019GL082411.

Zwally, H. J., Abdalati, W., Herring, T., Larson, K., Saba, J., and Steffen, K. Surface Melt-Induced Acceleration of Greenland Ice-Sheet Flow. *Science*, 297(5579):218–222, 2002. doi: 10.1126/science.1072708.